NUREG/CR-5948
LA-12459-MS

# Hydrogen Mixing Studies (HMS): Theory and Computational Model

Prepared by
T. L. Wilson, J. R. Travis

Los Alamos National Laboratory

Prepared for
U.S. Nuclear Regulatory Commission

## AVAILABILITY NOTICE

Availability of Reference Materials Cited in NRC Publications

Most documents cited in NRC publications will be available from one of the following sources:

1. The NRC Public Document Room, 2120 L Street, NW., Lower Level, Washington, DC 20555

2. The Superintendent of Documents, U.S. Government Printing Office, P.O. Box 37082, Washington, DC 20013-7082

3. The National Technical Information Service, Springfield, VA 22161

Although the listing that follows represents the majority of documents cited in NRC publications, it is not intended to be exhaustive.

Referenced documents available for inspection and copying for a fee from the NRC Public Document Room include NRC correspondence and internal NRC memoranda; NRC bulletins, circulars, information notices, inspection and investigation notices; licensee event reports; vendor reports and correspondence; Commission papers; and applicant and licensee documents and correspondence.

The following documents in the NUREG series are available for purchase from the GPO Sales Program: formal NRC staff and contractor reports, NRC-sponsored conference proceedings, international agreement reports, grant publications, and NRC booklets and brochures. Also available are regulatory guides, NRC regulations in the *Code of Federal Regulations*, and *Nuclear Regulatory Commission Issuances*.

Documents available from the National Technical Information Service include NUREG-series reports and technical reports prepared by other Federal agencies and reports prepared by the Atomic Energy Commission, forerunner agency to the Nuclear Regulatory Commission.

Documents available from public and special technical libraries include all open literature items, such as books, journal articles, and transactions. *Federal Register* notices, Federal and State legislation, and congressional reports can usually be obtained from these libraries.

Documents such as theses, dissertations, foreign reports and translations, and non-NRC conference proceedings are available for purchase from the organization sponsoring the publication cited.

Single copies of NRC draft reports are available free, to the extent of supply, upon written request to the Office of Administration, Distribution and Mail Services Section, U.S. Nuclear Regulatory Commission, Washington, DC 20555.

Copies of industry codes and standards used in a substantive manner in the NRC regulatory process are maintained at the NRC Library, 7920 Norfolk Avenue, Bethesda, Maryland, for use by the public. Codes and standards are usually copyrighted and may be purchased from the originating organization or, if they are American National Standards, from the American National Standards Institute, 1430 Broadway, New York, NY 10018.

## DISCLAIMER NOTICE

This report was prepared as an account of work sponsored by an agency of the United States Government. Neither the United States Government nor any agency thereof, or any of their employees, makes any warranty, expressed or implied, or assumes any legal liability of responsibility for any third party's use, or the results of such use, of any information, apparatus, product or process disclosed in this report, or represents that its use by such third party would not infringe privately owned rights.

NUREG/CR-5948
LA-12459-MS

# Hydrogen Mixing Studies (HMS): Theory and Computational Model

Prepared by
T. L. Wilson, J. R. Travis

Los Alamos National Laboratory

Prepared for
U.S. Nuclear Regulatory Commission

## AVAILABILITY NOTICE

Availability of Reference Materials Cited in NRC Publications

Most documents cited in NRC publications will be available from one of the following sources:

1. The NRC Public Document Room, 2120 L Street, NW., Lower Level, Washington, DC 20555

2. The Superintendent of Documents, U.S. Government Printing Office, P.O. Box 37082, Washington, DC 20013-7082

3. The National Technical Information Service, Springfield, VA 22161

Although the listing that follows represents the majority of documents cited in NRC publications, it is not intended to be exhaustive.

Referenced documents available for inspection and copying for a fee from the NRC Public Document Room include NRC correspondence and internal NRC memoranda; NRC bulletins, circulars, information notices, inspection and investigation notices; licensee event reports; vendor reports and correspondence; Commission papers; and applicant and licensee documents and correspondence.

The following documents in the NUREG series are available for purchase from the GPO Sales Program: formal NRC staff and contractor reports, NRC-sponsored conference proceedings, international agreement reports, grant publications, and NRC booklets and brochures. Also available are regulatory guides, NRC regulations in the *Code of Federal Regulations*, and *Nuclear Regulatory Commission Issuances*.

Documents available from the National Technical Information Service include NUREG-series reports and technical reports prepared by other Federal agencies and reports prepared by the Atomic Energy Commission, forerunner agency to the Nuclear Regulatory Commission.

Documents available from public and special technical libraries include all open literature items, such as books, journal articles, and transactions. *Federal Register* notices, Federal and State legislation, and congressional reports can usually be obtained from these libraries.

Documents such as theses, dissertations, foreign reports and translations, and non-NRC conference proceedings are available for purchase from the organization sponsoring the publication cited.

Single copies of NRC draft reports are available free, to the extent of supply, upon written request to the Office of Administration, Distribution and Mail Services Section, U.S. Nuclear Regulatory Commission, Washington, DC 20555.

Copies of industry codes and standards used in a substantive manner in the NRC regulatory process are maintained at the NRC Library, 7920 Norfolk Avenue, Bethesda, Maryland, for use by the public. Codes and standards are usually copyrighted and may be purchased from the originating organization or, if they are American National Standards, from the American National Standards Institute, 1430 Broadway, New York, NY 10018.

## DISCLAIMER NOTICE

NUREG/CR-5948
LA-12459-MS
R8

# Hydrogen Mixing Studies (HMS): Theory and Computational Model

Manuscript Completed: November 1992
Date Published: December 1992

Prepared by
T. L. Wilson, J. R. Travis*

Los Alamos National Laboratory
Los Alamos, NM 87545

**Prepared for**
**Division of Systems Research**
**Office of Nuclear Regulatory Research**
**U.S. Nuclear Regulatory Commission**
**Washington, DC 20555**
**NRC FIN A7247**

*Science Applications International Corporation
2109 Air Park Rd., SE
Albuquerque, NM 87106

**Abstract**

This report documents the governing physical equations and computational model of HMS (**H**ydrogen **M**ixing **S**tudies), a finite-volume computer code for solving transient, three-dimensional, compressible, Navier-Stokes equations for multiple gas species. The code is designed to be a best-estimate tool for predicting the transport, mixing, and combustion of hydrogen and other gases in nuclear reactor containments and other facilities. An analysis with HMS will result in the pressure and temperature loadings on the walls and internal structures.

HMS can model geometrically complex containment systems with multiple compartments and internal structures. It can calculate gas behavior of low-speed buoyancy-driven flows, of diffusion-dominated flows, and during deflagrations. The code can model condensation in the bulk fluid regions; heat transfer to walls and internal structures by convection, radiation and condensation; chemical kinetics of combustion of hydrogen or hydrocarbons; and fluid turbulence. Heat conduction within walls and structures is one-dimensional.

In HMS, the computational domain is discretized by a mesh of parallelepiped cells in either Cartesian or cylindrical geometry, where primary hydrodynamic variables are cell-face-centered normal velocity and cell-centered density, internal energy, and pressure. A linearized Arbitrary-Lagrangian-Eulerian (ALE) method is used for approximating the solution to the mass, momentum, and energy conservation equations.

CONTENTS

CONTENTS

## Executive Summary

Los Alamos National Laboratory is developing the Hydrogen Mixing Studies (HMS) code as a best-estimate tool for predicting transport, mixing, and combustion of hydrogen and other gases in nuclear reactor containments and other facilities. The code can model geometrically complex facilities with multiple compartments and internal structures. It can simulate the effects of condensation, heat transfer to walls and internal structures, chemical kinetics, and fluid turbulence. An analysis with the HMS code will result in the pressure and temperature loadings on the walls and internal structures participating in an event.

HMS has been used to calculate the distribution and control of hydrogen in complicated nuclear containment and confinement buildings and in non-nuclear facilities. It has been applied to situations involving transporting and distributing combustible gas mixtures. It has been used to study gas behavior in complicated containment systems, with low-speed buoyancy-driven flows, with diffusion-dominated flows, and during deflagrations. The effects of control of such mixtures by safety systems can be analyzed.

HMS is a finite-volume code based on proven computational fluid dynamics methodology that solves the compressible Navier-Stokes equations for 3D volumes in Cartesian or cylindrical coordinates. Wall shear stress models are provided for bulk laminar and turbulent flow. HMS has transport equations for multiple gas species and one for internal energy. The three turbulence models used in HMS—algebraic, subgrid scale, and $\kappa$-$\varepsilon$—are, respectively, zero-, one-, and two-transport-equation models that determine turbulent velocity and length scales needed to compute the turbulent viscosity. Terms for turbulent diffusion of different species are included in the mass and internal energy equations.

Heat conduction within walls and structures is one-dimensional. Heat and mass transport to walls and structures is based on a modified Reynolds analogy which accounts for increased heat transfer and condensation when the mass fraction of steam becomes a relatively large fraction of the mass of the gas mixture. Condensation can occur in the gaseous volumes or on the walls.

Chemical energy of combustion involving hydrogen or hydrocarbon fuels provides a source of energy within the gaseous regions. A one-step global chemical kinetics model based on a modified Arrhenius law accounts for local fuel and oxidizer concentrations. A simplified model is available for radiating a fraction of energy of combustion from a cell to surrounding walls or from hotter walls back to the gas, where the user supplies view factors and logical connections between cells and walls within a special subroutine.

In HMS, the computational domain is discretized by a mesh of rectangular parallelepiped cells in either Cartesian or cylindrical geometry, where primary hydrodynamic variables are cell-face-centered normal velocity and cell-centered density,

internal energy, and pressure. A linearized Arbitrary-Lagrangian-Eulerian (ALE) method is used for approximating the solution to the mass, momentum, and energy conservation equations.

In the 1980s the name HMS was applied to any of a series of codes developed to solve special problems of hydrogen mixing using a common theoretical basis. The latest version (HMS-92) is the first version that integrates the best features of all the older versions into a single software package. HMS-92 includes several improvements in models, calculational speed, input and output, and code structure.

(1) Vectorizing the entire code makes run 5 to 10 times faster than the old unvectorized code.

(2) Generalizing the problem setup replaces code hardwiring of boundary conditions, initial conditions and geometry (including obstacles) with highly flexible, cell-by-cell user input specifications.

(3) Changing the cell grid structure from a fixed size (with hardwired size changes) to variable sizing by input specification allows the grid structure to fit the geometry and analysis conditions correctly, effectively, and easily.

(4) Coupling to a more powerful graphics package (2D and 3D velocity vectors, 2D property contours, 1D property profiles and time histories) gives the user more control, capability and flexibility in specifying plotting during problem setup or in post processing.

(5) Adding a hydrogen burn model extends the capability for analyzing safety issues involving hydrogen mixing and combustion.

(6) Implementing the Los Alamos Memory Management System automates allocating memory and storage efficiently for the problem definition, freeing the user from this task.

(7) Modernizing the coding of the models and the data structures enhances the ability to modify the code efficiently.

HMS code documentation is currently planned for the following three volumes.

(1) HMS: Theory and Computational Model
(2) HMS: User's Guide
(3) HMS: Assessment Manual

The theory manual describes the fluid dynamics models, equations of state and constitutive relations, special component models, and numerical methods. The User's Guide, planned for 1993 publication, will describe the input needed to run HMS and provide guidance to the user on how to use the code.

The Assessment Manual, in preparation, will include the reports on the new developmental assessments performed with HMS-92 and will be expanded as more assessments become available. HMS-92 was recently assessed against three problems with known (experimental) results.

(1) von Karman Vortex Street. We have performed calculations on flow past obstacles at selected Reynolds numbers. The computed flow patterns agree well with experimental observations—specifically the occurrence of a vortex street (double row of vortices) at sufficiently high Reynolds numbers. The calculated non-dimensional vortex-shedding frequency agrees well with the empirical values.

(2) Sandia FLAME Facility. The Sandia FLAME Facility test F-21 involved injection of hydrogen horizontally and near the bottom into a long channel full of air. Because of the absence of operating fans to mix the gases, a buoyant plume developed and caused vertical stratification of the hydrogen. Two- and three-dimensional simulations of this experiment have been performed. Both calculations show a buoyant plume developing and, as a result, a stratification in hydrogen concentration, which are in good agreement with the experimental observations.

(3) HDR Facility. This assessment problem models the T31.5 experiment that simulates a large break LOCA and hydrogen release. The experiment was carried out in the HDR containment building, which is a full-scale facility with many compartments, interconnected passageways, and internal obstacles. The calculated results agree reasonably well with the experimental data.

Previous versions of HMS were applied to the following facilities and standard problems.

- EPRI/HDR International Standard Problems
- Sandia FLAME and VGES Facilities
- Nevada Hydrogen Tests
- NRC Containment Loads Working Group Standard Problems
- HCOG 1/4 Scale Test Facility
- CSNI Hydrogen Distribution Benchmark Problems
- Hydrogen Rule for large Dry Containments
- PHDR Large-Scale Hydrogen Mixing Experiment
- PHDR Fire Experiments

## Acknowledgment

The authors would like to thank John Dukowicz for his help in the implementation of the Conjugate Residual algorithm. We also thank Juanita Lujan for her careful preparation of the manuscript.

## Nomenclature

| | |
|---|---|
| $A_w$ | Wall area |
| $\mathbf{b}$ | Velocity of control surface |
| $C_D$ | Structural drag coefficient |
| $C_f$ | Frequency (or pre-exponential) factor—see Eq. (60) |
| $C_p$ | Specific heat at constant pressure |
| $C_v$ | Specific heat at constant volume |
| $\mathbf{D}$ | Structural drag vector |
| E | Activation energy |
| $\mathbf{g}$ | Gravitational vector |
| $h_w$ | Wall heat-transfer coefficient |
| $h_\alpha$ | Enthalpy for species $\alpha$ |
| $H_2$ | Hydrogen |
| $H_2O$ | Water vapor |
| i | x (or r)-direction index |
| I | specific internal energy |
| $I_o$ | Specific internal energy at reference temperature |
| j | y (or $\theta$)-direction index |
| k | z-direction index |
| $\ell$ | Turbulence length scale |
| m | Mass |
| M | Molecular weight |
| n | Steam mole fraction |
| $\mathbf{n}$ | Unit normal vector |
| $N_2$ | Nitrogen |
| $O_2$ | Oxygen |
| p | Pressure |
| Q | Energy source or sink |
| $Q_c$ | Energy of combustion |
| $Q_w$ | Convected energy exchange with walls |
| $\mathbf{q}$ | Energy flux vector |
| $q_c$ | Energy lost or transferred to structures by condensation |
| $q_r$ | Radiated energy to wall surface |
| $q_w$ | Convected energy to wall surface |
| $q_{wr}$ | Radiated energy from wall surface |
| r | Radial coordinate |
| R | Flux ratio |
| $R_a$ | Gas constant |
| $\Re$ | Universal gas constant |
| S | Mass source or sink |
| $S^*$ | Moving control surface |
| $S_\Phi$ | Arbitrary source term |
| t | Time |
| T | Temperature |

| | |
|---|---|
| $u$ | x (or r)-direction velocity component |
| $\mathbf{u}$ | Fluid velocity vector |
| $\mathbf{u}_g$ | Grid velocity vector |
| $v$ | y (or θ)-direction velocity component |
| $V$ | Volume |
| $V^*$ | Moving control volume |
| $w$ | z-direction velocity component |
| $\mathbf{x}$ | Position vector |
| $x$ | Cartesian coordinate |
| $x_\alpha$ | Mass fraction |
| $y$ | Cartesian coordinate |
| $y_c$ | Distance from wall to cell center |
| $z$ | Cartesian coordinate |
| $\beta$ | Wall thermal diffusivity |
| $D$ | Apparent or total mass diffusivity |
| $\delta x$ | Mesh cell size for heat conduction grid |
| $\Delta t$ | Time step |
| $\varepsilon$ | Emissivity, dissipation of turbulent kinetic energy |
| $\kappa$ | Turbulent kinetic energy |
| $\lambda$ | Second coefficient of apparent or total viscosity |
| $\mu$ | First coefficient of apparent or total viscosity |
| $\nu$ | Apparent or total kinematic viscosity |
| $\rho$ | Density |
| $\sigma$ | Stefan-Boltzman constant |
| $\tau$ | Viscous stress tensor |
| $\theta$ | Azimuthal coordinate |
| $\dot{\omega}$ | Reaction rate |
| $\phi$ | Apparent or total conductivity |
| $\Phi$ | Arbitrary scalar or vector function |
| $\phi_T$ | Rate factor |
| $\Theta_m$ | Mass-transfer correction factor |
| $\Theta_T$ | Heat-transfer correction factor |

**Superscripts**

| | |
|---|---|
| A | Lagrangian phase A computational level |
| B | Lagrangian phase B computational level |
| n | Old time level |
| n+1 | New time level |
| * | moving control surface or volume |

**Subscripts**

| | |
|---|---|
| b | Bulk fluid property |

| | |
|---|---|
| c | Chemical energy |
| f | cell face |
| F | Fuel |
| g | Gas |
| i | x (or r)-direction index |
| j | y (or $\theta$)-direction index |
| k | z-direction index |
| m | Momentum control volume |
| o | Oxidizer, reference |
| 0 | Reference |
| r | Radiated energy |
| ref | Reference |
| s | Steam at structure surface |
| w | Wall |
| $\alpha$ | Species |

# 1 INTRODUCTION

## 1.1 Background

Combustion in light-water reactor (LWR) containments can cause high pressures or temperatures that can, in turn, damage a containment or affect important safety-related equipment. After the Three-Mile Island Accident (a severe, or degraded-core, accident), it was found that significant quantities of hydrogen had been generated from the chemical reaction between the zirconium cladding (the thin protective covering of the nuclear fuel) and the water vapor. When released into the containment, this hydrogen burned by one or more combustion modes and threatened the containment integrity, internal structures, and safety-related equipment.

Modeling the geometries of containment buildings is difficult. One example is the Heiss Dampf Reactor (HDR) containment near Frankfurt, West Germany; shown in Fig. 1. The HDR building is 60 m high and 20 m in diameter. It contains two stairwells, an elevator shaft, several vertical open hatchways, and about 70 rooms. This particular containment has roughly 11,300 $m^3$ of free volume, or approximately one-sixth the free volume of a typical US pressurized water reactor (PWR) containment. Experiments simulating cable tray and hydrocarbon lubricating oil fires, and severe accident combustion phenomena currently are being conducted.

The US Nuclear Regulatory Commission (NRC) has supported research at the Los Alamos and Sandia National Laboratories to develop combustion models to evaluate fire threats to the reactor containment and safety-related equipment. Current research will coordinate model validation with ongoing experiments at the HDR facility. We will describe the Los Alamos field-model approach in the report.

## 1.2 Computational Methodology

This report documents the theoretical and computational aspects of HMS (**H**ydrogen **M**ixing **S**tudies), a finite-volume computer code for solving transient, three-dimensional, compressible, Navier-Stokes equations for multiple gas species. The code is designed to be a best-estimate tool for predicting the transport, mixing, and combustion of hydrogen gas in nuclear reactor containments. HMS is based on the governing physical laws and modeling assumptions that are described in the Sec. 2. In Sec. 3, we describe the linearized ICEd-ALE (**I**mplicit **C**ontinuous-Fluid **E**ulerian; **A**rbitrary-**L**agrangian-**E**ulerian) computational method used to integrate the equations in time and space. Briefly, each computational step is divided into three phases.

(1) An explicit Lagrangian phase computes changes in material volume, density, velocity, and internal energy caused by pressure gradients, combustion, condensation, heat conduction, and turbulence.

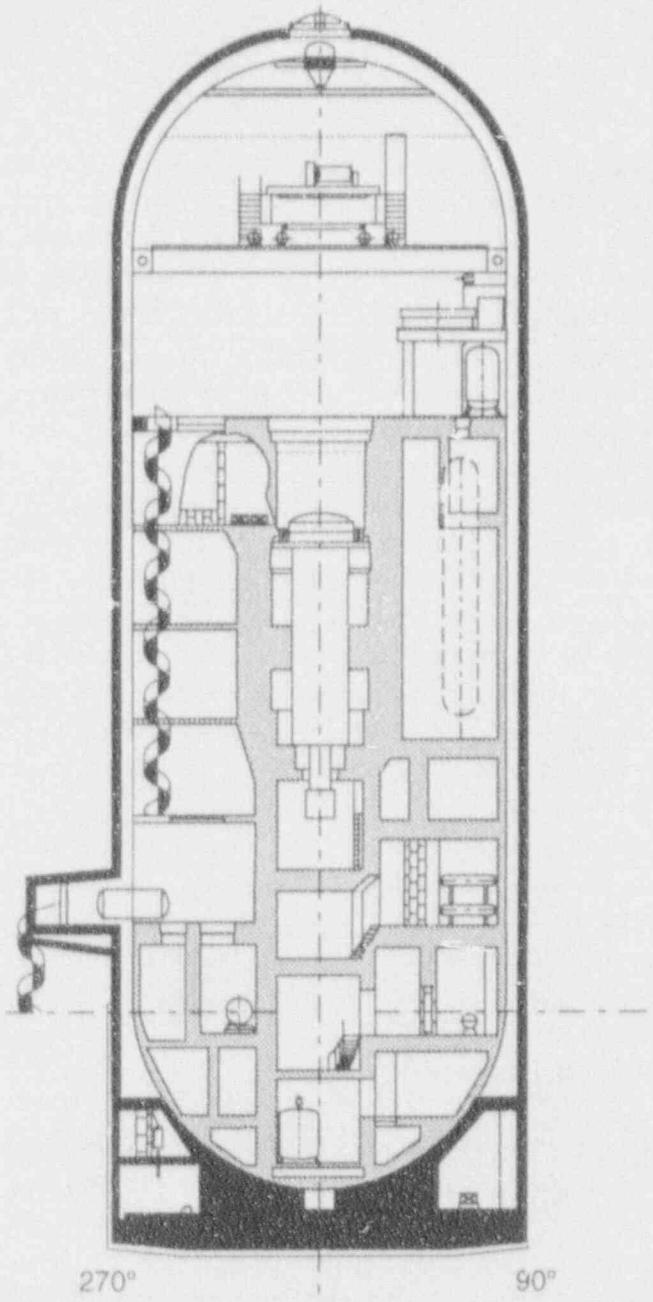


Figure 1 Cross-section of the Heiss Dampf Reactor (HDR) near Frankfurt, Germany.

(2) An implicit Lagrangian phase calculates pressures at the advanced time level by solving simultaneously for pressure, density, velocity, and internal energy.

(3) A rezone phase computes the mass, momentum, and energy exchange between Eulerian cells that has occurred in the Lagrangian phase and repartitions these variables onto the original mesh.

Turbulence quantities—kinetic energy, dissipation, and viscosity—are calculated explicitly at the end of each time step. One-dimensional heat conduction through structural components is computed to accurately account for the energy transfer across gas-structure interfaces.

## 2 MATHEMATICAL AND PHYSICAL MODELS

The equations of motion for a compressible fluid are derived from the physical laws that require the conservation of mass, momentum, and energy. The equations of change, which are presented in this section, relate the dynamics of the fluid to temporal and spatial influences such as viscous stress, body force, turbulence, structural resistance, heat transfer, condensation, and combustion. This includes relations for the transport of individual gas species. An equation of state is included to relate pressure ($p$) to density ($\rho$) and internal energy ($I$).

As suggested by the "ALE" name, HMS uses both the Lagrangian and Eulerian viewpoints. The Lagrangian (or material) specification considers specific elements of matter and describes the motion as functions of space ($\mathbf{x}$) and time ($t$). This viewpoint is useful because the conservation laws refer to specific parcels of matter. However, the Eulerian (or spatial) viewpoint is often more convenient because it describes flow in terms of volumes fixed in space. Because the computational method used to model the flow is facilitated by dividing the problem domain into parallelepiped Eulerian volumes (cells) in either cartesian or cylindrical geometry, it is natural to present the continuous equations in integral form (Refs. 1 and 2). This makes it easier to see how the integration of continuous volume and surface integrals presented in this section are approximated by the discrete or finite-volume equations give in Sec. 3.

### 2.1 The Generalized Conservation Equation

The conservation of any arbitrary extensive variable (for example, mass, momentum, or energy) is

$$\frac{d}{dt}\int_V \Phi \, dV = \int_V S_\Phi dV \tag{1}$$

where $\Phi(\mathbf{x}, t)$ is any continuously summable function, V is a material volume, and $S_\Phi$ is a source term. Using the Reynolds Transport Theorem, this may be expressed as

$$\int_V \frac{\partial \Phi}{\partial t}\, dV + \int_S \Phi\,(\mathbf{u}\cdot\mathbf{n})\, dA = \int_V S_\Phi dV \tag{2}$$

where $\mathbf{u}(\mathbf{x}, t)$ is the fluid velocity and $\mathbf{n}$ and dA are the outward unit normal vector and differential area, respectively, of material surface S bounding V. Applying the transport theorem to an arbitrary control volume V* (Ref. 2) (not necessarily a material volume) enclosed by surface S* gives

$$\frac{d}{dt}\int_{V^*} \Phi \, dV = \int_{V^*} \frac{\partial \Phi}{\partial t} \, dV + \int_{S^*} \Phi \, (\mathbf{b} \cdot \mathbf{n}) \, dA + \int_{V^*} S_\Phi dV \tag{3}$$

If V* is chosen to be instantaneously coincident with V, Eqs. (2) and (3) may be combined to give

$$\frac{d}{dt}\int_{V^*} \Phi \, dV = \int_{S^*} \Phi \, (\mathbf{b} - \mathbf{u}) \cdot \mathbf{n} \, dA + \int_{V^*} S_\Phi dV \tag{4}$$

the integral form of the generalized conservation law. This is the basic kinematic relation used in the following three subsections and states that the time-rate-of-change of $\Phi$ in an arbitrary control volume V* (left side) is equal to the inflow of $\Phi$ through the boundary plus the source term (right side). The term $\mathbf{b} - \mathbf{u}$ is the relative velocity between the control surface and the fluid. When $\mathbf{b} = \mathbf{u}$, we recover the Lagrangian form [Eq. (1)]. For a control volume that is fixed with respect to the coordinate axes, $\mathbf{b} = 0$ and we recover the Eulerian form

$$\frac{d}{dt}\int_{V} \Phi \, dV = -\int_{S} \Phi \, (\mathbf{u} \cdot \mathbf{n}) \, dA + \int_{V} S_\Phi dV \tag{5}$$

or

$$\int_{V} \frac{\partial \Phi}{\partial t} \, dV = -\int_{S} \Phi \, (\mathbf{u} \cdot \mathbf{n}) \, dA + \int_{V} S_\Phi dV \tag{6}$$

### 2.2 The Mass Conservation Equations

The mixture mass conservation equation follows directly from Eq. (4) by letting $\Phi = \rho$

$$\frac{d}{dt}\int_{V^*} \rho \, dV = \int_{S^*} \rho \, (\mathbf{b} - \mathbf{u}) \cdot \mathbf{n} \, dA + \int_{V^*} S_\rho \, dV \tag{7}$$

where $\rho$ is the mixture density or the sum of the macroscopic densities for each individual species, $\mathbf{u}$ is the mass-average velocity vector, and $S_\rho$ is the mass loss (condensation) per unit volume and time. Similarly, setting $\Phi = 1$ in Eq. (4) gives an expression for the change in volume

$$\frac{dV}{dt} = \int_{S^*} \mathbf{b} \cdot \mathbf{n} \, dA \tag{8}$$

The transport equation for individual species is given by

$$\frac{d}{dt}\int_{V^*} \rho_\alpha \, dV = \int_{S^*} \rho_\alpha \, (\mathbf{b} - \mathbf{u}) \cdot \mathbf{n} \, dA + \int_{V^*} \nabla \cdot \left[ \rho \mathcal{D} \, \nabla \left( \frac{\rho_\alpha}{\rho} \right) \right] dV + \int_{V^*} S_\alpha \, dV \tag{9}$$

where $\alpha$ denotes the gas species, $\rho_\alpha$ is the mass per unit volume (macroscopic density), D is the mass diffusivity coefficient, and the source or sink term, $S_\alpha$, represents the species mass created or destroyed by chemical reactions and the loss of steam as a result of condensation. The diffusion of species $\alpha$ is represented by the second integral on the right side of Eq. (9). When Eq. (9) is summed over all species, the result is the mixture mass [Eq. (7)].

### 2.3 The Momentum Transport Equations

The mixture-momentum conservation equations are given by

$$\frac{d}{dt}\int_{V^*} \rho \mathbf{u} \, dV = \int_{S^*} \rho \mathbf{u} \, (\mathbf{b} - \mathbf{u}) \cdot \mathbf{n} \, dA + \int_{V^*} [ -\nabla p + \rho \mathbf{g} ] \, dV - \int_{S^*} (\tau \cdot \mathbf{n}) dA + \int_{S_s} \mathbf{D} \, dA_s \tag{10}$$

where p is the pressure, $\tau$ is the viscous stress tensor, $\mathbf{g}$ is the gravitational vector, and $\mathbf{D}$ is the internal structure drag vector. The right-side integrals represent, respectively, the flux of momentum through the control surface, the sum of pressure gradient, gravity, and viscous forces on the control volume, and fluid drag forces acting on structural surfaces.

The cartesian and cylindrical components of $\tau$ for a Newtonian fluid are given in Tables 1 and 2, respectively. The components of $\mathbf{u}$ are (u, v, w) in the x-, y-, and

z-directions (cartesian coordinates) or r-, θ-, and z-directions (cylindrical coordinates) and subscripts on τ indicate the surface normal direction and the direction of the stress component.

The coefficient of viscosity, μ, is interpreted as an "apparent" or "turbulent" viscosity. Here we have used the second viscosity coefficient, $\lambda = -2\mu/3$, which is equivalent to assuming the bulk viscosity to be zero. The calculation of the apparent viscosity through the turbulence model will be discussed in Sec. 2.7.

**Table 1 Stress tensor components for a Newtonian fluid (cartesian coordinates)**

$$\tau_{xx} = -\mu\left[2\frac{\partial u}{\partial x} - \frac{2}{3}(\nabla\cdot\mathbf{u})\right] \qquad \tau_{xy} = -\mu\left[\frac{\partial u}{\partial y} + \frac{\partial v}{\partial x}\right]$$

$$\tau_{yy} = -\mu\left[2\frac{\partial v}{\partial y} - \frac{2}{3}(\nabla\cdot\mathbf{u})\right] \qquad \tau_{xz} = -\mu\left[\frac{\partial u}{\partial z} + \frac{\partial w}{\partial x}\right]$$

$$\tau_{zz} = -\mu\left[2\frac{\partial w}{\partial z} - \frac{2}{3}(\nabla\cdot\mathbf{u})\right] \qquad \tau_{yz} = -\mu\left[\frac{\partial v}{\partial z} + \frac{\partial w}{\partial y}\right]$$

**Table 2 Stress tensor components for a Newtonian fluid (cylindrical coordinates)**

$$\tau_{rr} = -\mu\left[2\frac{\partial u}{\partial r} - \frac{2}{3}(\nabla\cdot\mathbf{u})\right] \qquad \tau_{r\theta} = -\mu\left[r\frac{\partial}{\partial r}\left(\frac{v}{r}\right) + \frac{1}{r}\frac{\partial u}{\partial \theta}\right]$$

$$\tau_{\theta\theta} = -\mu\left[2\left(\frac{1}{r}\frac{\partial v}{\partial \theta} + \frac{u}{r}\right) - \frac{2}{3}(\nabla\cdot\mathbf{u})\right] \qquad \tau_{z\theta} = -\mu\left[\frac{\partial v}{\partial z} + \frac{1}{r}\frac{\partial w}{\partial \theta}\right]$$

$$\tau_{zz} = -\mu\left[2\frac{\partial w}{\partial z} - \frac{2}{3}(\nabla\cdot\mathbf{u})\right] \qquad \tau_{rz} = -\mu\left[\frac{\partial u}{\partial z} + \frac{\partial w}{\partial r}\right]$$

## 2.4 The Internal Energy Transport Equation

The equation of change for total internal energy is

$$\frac{d}{dt}\int_{V^*}\rho I\,dV = \int_{S^*}\rho\bar{I}\,(\mathbf{b}-\mathbf{u})\cdot\mathbf{n}\,dA - \int_{V^*}\left[p\nabla\cdot\mathbf{u} + \frac{p}{V}\frac{\partial V_s}{\partial t}\right]dV + \int_{S^*}\mathbf{q}\cdot\mathbf{n}\,dA + \int_{V^*}Q\,dV \tag{11}$$

where I is the mixture specific internal energy and Q is the energy source or sink per unit volume and time as a result of combustion, condensation, and energy exchange with internal structures, floors, ceilings, and walls. Because condensation effects can dominate the $p\nabla\cdot\mathbf{u}$ work term, we must account for the remaining gas in a computational cell expanding into the volume change associated with the condensate. We account for this effect by using the ideal gas equation of state to arrive at

$$\frac{1}{V}\frac{\partial V_s}{\partial t} = \frac{R_{H_2O}T}{V_c p}\sum_i \dot{m}_i = -\frac{R_{H_2O}T}{p}S \tag{12}$$

where $R_{H_2O}$ is the gas constant for steam, T is the gas mixture temperature, $V_s$ is the steam volume, and $\sum_i \dot{m}_i$ is the sum of all mass per unit time of steam condensing on all surfaces internal to or bounding the computational cell $V_c$. Note that S is the same mass loss per unit volume and time as Eq. (7). The energy flux vector $\mathbf{q}$, is given by

$$\mathbf{q} = \phi\nabla T + \rho\mathcal{D}\sum_\alpha h_\alpha \nabla\left(\frac{\rho_\alpha}{\rho}\right) \tag{13}$$

where $\phi$ is the apparent or turbulent conductivity, D is the apparent or turbulent mass diffusivity, and $h_\alpha$ is the enthalpy for species $\alpha$.

## 2.5 Constitutive Relationships

The specific internal energy of specie $\alpha$ is related to the temperature by

$$I_\alpha = (I_o)_\alpha + \int_{T_o}^{T}(C_v)_\alpha\,dT \tag{14}$$

For the species in which we are most interested ($O_2$, $N_2$, $H_2$, and $H_2O$), we can approximate the specific heats by

$$(C_v)_\alpha = a_0 + a_1T + a_2T^2 + a_3T^3 + a_4T^4 \tag{15}$$

where the $a_i$'s are specie-dependent coefficients (Ref. 3).

After integrating Eq. (14), the specific internal energy as a function of temperature is approximated with the quadratic function

$$I_\alpha = A_\alpha T^2 + B_\alpha T + C_\alpha \tag{16}$$

over the temperature range 200–2500 K. The total specific internal energy then is given by

$$I = \sum_\alpha x_\alpha I_\alpha \tag{17}$$

where $x_\alpha$ is the mass fraction for species $\alpha$.

For consistency with Eq. (16), we approximate each species' specific heat by differentiating Eq. (16) with respect to temperature to yield

$$(C_v)_\alpha = 2A_\alpha T + B_\alpha \tag{18}$$

instead of applying Eq. (15) directly.

Pressure, p, is obtained by applying the Gibbs-Dalton law of partial pressures to an ideal gas mixture

$$p = T\sum_\alpha R_\alpha \rho_\alpha = \rho T \sum_\alpha x_\alpha R_\alpha \tag{19}$$

where $R_\alpha$ is the gas constant for species $\alpha$. The constant-pressure specific heats are calculated by

$$(C_p)_\alpha = R_\alpha + (C_v)_\alpha \tag{20}$$

## 2.6 Heat-Transfer and Condensation Relationships

### 2.6.1 Gas–Structure Heat Transfer

The heat exchange, $Q_w$, between the gas mixture and a solid boundary (referred to generically as a wall, but it may in fact be a ceiling, floor, or internal structure) is given by

$$Q_w = q_w / V_c \tag{21}$$

where

$$q_w = h_w A_w (T_w - T_g) \tag{22}$$

In these expressions, $V_c$ is the computational cell volume, $T_w$ is the structure surface temperature, $T_g$ is the gas temperature, $h_w$ is the heat-transfer coefficient between the gas mixture and the internal structures, and $A_w$ is the cell face area for walls or the exposed area for internal structures in a computational cell.

The thermal boundary layer is taken into account by using a modified Reynolds analogy formulation (Ref. 4), which is simplified to obtain the heat-transfer coefficient

$$h_w = \frac{\tau_w}{u_c} C_p \tag{23}$$

The rates of heat transfer and condensation increase when the mass fraction of steam becomes a relatively large fraction of the mass of the gas mixture. As the mass-transfer rate increases, the thermal and concentration boundary layers become thinner because of the suction effect of the condensation process. This reduction in the boundary layer thickness further increases the temperature and concentration gradients near the boundary and consequently increases the heat- and mass-transfer coefficients. Bird, Stewart, and Lightfoot (Ref. 5) (Sec. 21.5) develop correction factors based on film theory that can be used to determine the increase in the heat- and mass-transfer coefficients. The corrected heat-transfer coefficient then becomes

$$h_w^* = \Theta_T h_w \tag{24}$$

where

$$\Theta_T = \frac{\phi_T}{e^{\phi_T} - 1} \tag{25}$$

and the rate factor, $\phi_T$, is given by

$$\phi_T = \frac{-\dot{m}_w (C_p)_v}{h_w A_w} \tag{26}$$

where $\dot{m}_w$ is the wall condensation rate and $(C_p)_v$ is the specific heat of the water vapor at constant pressure. Note that in the presence of condensing water vapor, $\phi_T$ is negative, which increases the correction factor, $\Theta_T$, and the heat-transfer coefficient, $h_w^*$. The internal structure heat-transfer coefficient is computed in an analogous fashion.

### 2.6.2 Condensation

Condensation can occur on any structural surface (walls, ceiling, floors, and internal structures) provided the surface temperature is less than the saturation temperature of the water vapor next to the surface. The amount of energy resulting from condensation delivered to the wall surface area, $A_w$, is

$$q_c = \dot{m}_w \left[ (I_{H_2O})_b - (I_{H_2O})_s \right] \tag{27}$$

where $(I_{H_2O})_b$ is the specific internal energy of the water vapor in the computational cell adjacent to the wall with volume $V_c$ and $(I_{H_2O})_s$ is the specific internal energy of the liquid water film that is on the surface. (Note: we have taken the film temperature to be equal to the surface temperature of the wall.)

Actually, the term in brackets in Eq. (27) states that the energy per unit mass deposited on the surface caused by condensation is

$$(I_{H_2O})_b - (I_{gs})_s + h_{fg} + (I_{fg})_s - (I_{H_2O})_s \tag{28}$$

where $(I_{gs})_s$ is the specific internal energy at the saturation temperature of the water vapor, $h_{fg}$ is the latent heat of condensation, and $(I_{fg})_s$ is the specific internal energy at the saturation temperature for the liquid film.

The condensation rate is described as

$$\dot{m}_w = h_d^* A_w \left[ (\rho_{H_2O})_b - (\rho_{H_2O})_s \right] \tag{29}$$

where $h_d^*$ is the corrected mass-transfer coefficient, $(\rho_{H_2O})_b$ is the water vapor density in the bulk, and $(\rho_{H_2O})_s$ is the water vapor density on the condensing surface.

The mass-transfer coefficient, $h_d$, then can be expressed in terms of the heat-transfer coefficient, h (Ref. 6), as

$$h_d = \frac{h}{\rho C_p} \tag{30}$$

Following similar ideas as with the heat-transfer coefficient for relatively large steam mass fractions, we correct the mass-transfer coefficient by

$$h_d^* = \Theta_m h_d \tag{31}$$

where

$$\Theta_m = \frac{\log(R+1)}{R} \tag{32}$$

and

$$R = \frac{n_w - n_b}{1 - n_w} \tag{33}$$

is the flux ratio, $n_w$ is the steam mole fraction at the wall, and $n_b$ is the steam mole fraction in the bulk.

### 2.6.3. Radiation

We model the radiation heat transfer in a relatively simple fashion. We assume that 15% of the total chemical energy of combustion is radiated from a point source at the computational cell center.* This energy is radiated spherically away from each computational cell where combustion occurs to solid surfaces such as floors, ceilings, and walls with the appropriate geometric view factors. In some cases, such as the hydrogen diffusion flames in the Mark III containments (Ref. 7), the wet-well walls become quite hot, and energy is reradiated from each wall segment by

$$q_{wr} = A_w \sigma(\varepsilon_w T_w^4 - T_{ref}^4) \tag{34}$$

where $\sigma$ is the Stefan-Boltzmann constant, $\varepsilon_w$ is the wall emissivity, and $T_{ref}$ is the reference temperature.

---

* B. Zalosh, Factory Mutual Corporation, "Energetics of Hydrogen Combustion," personal communication (1984).

### 2.6.4 Heat Conduction

For every computational cell side interfacing with a wall, ceiling, or floor, the one-dimensional transient heat-conduction equation

$$\frac{\partial T}{\partial t} = \beta \frac{\partial^2 T}{\partial x^2} \tag{35}$$

with the wall boundary condition

$$q_w + q_c + \sum q_r - q_{wr} = -kA_w \left.\frac{\partial T}{\partial x}\right|_{x=0} \tag{36}$$

is solved from the temperature distribution, $T(x)$, and the wall surface temperature, $T_w$. $\beta$ in Eq. (35) is the thermal diffusivity of the wall. On the left side of Eq. (36), the four terms represent energy delivered to a wall section by convection, condensation, radiation from all computational cells with combustion occurring in line-of-sight contact, and reradiation of energy from hot surfaces, respectively. To simplify the reradiated energy analysis, we have assumed this energy to be deposited in the surrounding gas.

### 2.6.5 Wall Shear Stress

The heat-transfer coefficient expression [Eq. (23)] contains the computational cell-centered average velocity, $u_c$, and the wall shear stress, $\tau_w$, which is related to the fluid density and the wall shear speed $u_*$ by

$$\tau_w = \rho u_*^2 \tag{37}$$

We are unable to resolve turbulent boundary layers near solid walls with any practical computing mesh, so we match our solution near solid boundaries or internal structures with the turbulent law-of-the-wall (Ref. 8)

$$\frac{u_c}{u_*} = A \log\left(y_c u_* / \nu\right) + B \tag{38}$$

This expression requires an iterative solution for $u_*$. We find that it is more convenient and almost as accurate to use an approximation obtained by replacing $u_*$ in the argument of the logarithm in Eq. (38) by the one-seventh-power law (Ref. 9). The one-seventh-power law may be rearranged to give

$$\frac{y_c u_*}{n} = 0.15\left(y_c u_c / \nu\right)^{7/8} \tag{39}$$

which yields

$$\frac{u_c}{u_*} = 2.19 \log\left(y_c u_c / \nu\right) + 0.76 \tag{40}$$

when substituted into Eq. (38) and when A = 2.5 and B = 5.5. It is now straightforward to find the shear speed, $u_*$, where $y_c$ is the distance from the wall to the cell-centered average speed, $u_c$, and $\nu$ is the gas mixture molecular kinematic viscosity.

The local Reynolds number, $(y_c u_c/\nu)$, may be small, indicating that the cell center lies in the laminar sublayer and the law-of-tne-wall formulation is not valid. In this case, Eq. (40) is replaced by the corresponding laminar formula

$$\frac{u_c}{u_*} = \left(y_c u_c / \nu\right)^{1/2} \tag{41}$$

The transition between Eqs. (40) and (41) is made at the value where they predict the same $u_*$, which is $(y_c u_c/\nu) = 130.7$. Therefore, $u_*$ is calculated by Eq. (40) when $(y_c u_c/\nu) \geq 130.7$ and by Eq. (41) when $(y_c u_c/\nu) < 130.7$. In the laminar case, the wall heat-transfer coefficient [Eq. (23)] reduces to $h_w = \rho\nu / y_c$, which results in a simple difference approximation to the laminar heat flux for a molecular Prandtl number of unity when substituted into Eq. (22).

### 2.7 Turbulence Modeling

Most flows of engineering interest, including the flows of concern here, are turbulent. Turbulence may be described qualitatively as the superposition of an irregular fluctuating motion on the mean flow, which, for an arbitrary variable $\psi$, may be expressed as

$$\psi = \overline{\psi} + \psi' \tag{42}$$

where, $\psi$ is the instantaneous value, $\psi'$ is the fluctuating (turbulent) component, and $\overline{\psi}$ is the mean value defined as

$$\overline{\psi} = \lim_{t \to \infty} \frac{1}{t} \int_{t_0}^{t_0+t} \psi \, dt \tag{43}$$

In practice, t is taken to be much larger than the characteristic times associated with $\psi'$.

When the instantaneous values of p, $\rho$, $\mu$, and $u_i$ ($u_i \equiv u, v, w$ for i = 1, 2, 3) are substituted into the mixture-momentum equations [Eq. (10)], the resulting equations

contain additional products of terms involving $u_i'$, $\overline{u_i}$, $\rho'$, and $\bar{\rho}$. The terms $-\bar{\rho}\overline{u_i'u_j'}$, called the Reynolds stresses, are the focus of attention in the turbulent equations. [Other correlations such as $\overline{u_i}\overline{\rho'u_j'}$ are discussed, for example, by Cebeci and Smith (Ref. 10) (Chap. 2).] Defining $-\bar{\rho}\overline{u_i'u_j'}$ as the components of the turbulent stress tensor $\tau_t$ and combining them with the laminar viscous stress, $\bar{\tau}$, the total stress tensor may be written as

$$\tau = \bar{\tau} + \tau_t \tag{44}$$

The effect of $\tau_t$ in most flows is a large increase in the apparent (turbulent) resistance of the flow; in other words, $\tau_t$ results in increased momentum transport. With the addition of the unknown turbulence quantities, Eqs. (7), (10), and (11) no longer form a closed set and modeling $\tau_t$ becomes the major problem in simulating turbulent motion.

To understand the general approach to modeling $\tau_t$, it is useful to consider two observations about the eddies that characterize the turbulent motion. First, the largest eddies (whose size is determined by the geometry of the flow) carry most of the turbulent kinetic energy. The smallest eddies, with sizes determined by molecular viscosity, dissipate turbulent kinetic energy. The qualitative dynamics of the eddies and their interaction with the mean flow are described by Rodi (Ref. 11).

> The large eddies interact with mean flow (because the scales of both are similar), thereby extracting kinetic energy from the mean motion and feeding it into the large-scale turbulent motion. The eddies can be considered as vortex elements which stretch each other. Due to this vortex stretching, which is an essential feature of the turbulent motion, the energy is passed on to smaller and smaller eddies until viscous forces become active and dissipate the energy. This process is called energy cascade. The rate at which mean-flow energy is fed into the turbulent motion is determined by the large-scale motion; only this amount of energy can be passed on to smaller scales and finally be dissipated. Therefore, the rate of energy dissipated is also determined by the large-scale motion although dissipation is a viscous process and takes place at the smallest eddies. It is important to note that viscosity does not determine the amount of dissipated energy but only the scale at which dissipation takes place. The smaller the effective viscosity (i.e. the larger the Reynolds number), the smaller are the dissipative eddies relative to the large-scale eddies. When buoyancy forces are present, there is also an exchange between potential energy of the mean flow and turbulent kinetic energy, which can go in both directions but is also effected through the large-scale motion.

The preceding observations are the basis for modeling the effects of turbulence on the mean flow, specifically in choosing the relevant velocity and length scales that characterize the local state of turbulence. Postulating an analogy between laminar stresses and Reynolds stresses (Boussinesq's idea), that is

$$\left(\tau_{ij}\right)_t = -\overline{\rho u_i' u_j'} = \mu_t \frac{\partial u_i}{\partial x_j} \tag{45}$$

the turbulence closure problem is seen as one of finding a turbulent or eddy viscosity $\mu_t$. The effects of turbulence on the mean flow come down to modeling $\mu_t$ (hereafter we drop the subscript t) as a function of fluid properties, the dynamics of the flow, and the geometry. The three turbulence models used in HMS—algebraic, subgrid scale, and $\kappa$ - $\varepsilon$—are, respectively, zero, one, and two transport equation models that predict the velocity and length scales that are used to compute $\mu$. The models are described in order of increasing complexity, number of equations, and computational effort and, as a rule, in order of accuracy.

Turbulence effects in the vicinity of a wall are modeled with the law-of-the-wall formulation (Sec. 2.6.5).

### 2.7.1 Algebraic Model

For a turbulent velocity scale Prandtl suggested that the square root of the mean turbulent kinetic energy $\kappa$ as a natural choice, where

$$\kappa = \frac{1}{2}\left(\overline{u'^2} + \overline{v'^2} + \overline{w'^2}\right)^{1/2} \tag{46}$$

and a length scale $\ell$ characteristic of the size of the energy carrying eddies. Thus,

$$\mu = C_\mu \rho \kappa^{1/2} \ell \tag{47}$$

where $C_\mu$ is a constant (typically 0.05). It often is estimated that 10% or less of the mean flow energy is contained in the turbulent kinetic energy, so

$$\kappa^{1/2} = \left[0.1(1/2)u^2\right]^{1/2} \tag{48}$$

For containment studies, the length scale usually is set equal to 0.25–0.5 m.

### 2.7.2 Subgrid Scale Model

This model also uses $\kappa^{1/2}$ as the characteristic velocity scale, but here $\kappa$ represents the turbulent kinetic energy of eddies too small to be resolved by the computational

mesh. By implication, the mesh size is the length scale; generally, we have set $\ell$ to be the length of the cell diagonal

$$\ell = \left(\Delta x^2 + \Delta y^2 + \Delta z^2\right)^{1/2} \tag{49}$$

The transport equation for the product $\rho\kappa$ is given by

$$\frac{d}{dt}\int_{V^*} \rho\kappa \, dV = \int_{S^*} \left[\rho\kappa(\mathbf{b}-\mathbf{u}) + (\mu\nabla\kappa)\right] \cdot \mathbf{n} \, dA$$

$$-\frac{2}{3}\rho\kappa \int_{S^*} (\mathbf{u}\cdot\mathbf{n}) \, dA \quad + \quad \int_{V^*} \left[\tau{:}\nabla\mathbf{u} - \frac{\rho\kappa^{3/2}}{\ell}\right] dV \tag{50}$$

where the first integral on the right-hand side represents the convection of turbulence by the established velocity field and the diffusion of turbulence, the second integral represents the effects of turbulence generation by compression, and the terms under the third integral represent production of turbulence by viscous dissipation and decay of turbulent energy into thermal energy. This last term appears with an opposite sign as a source term in the thermal internal energy density equation [Eq. (11)]. Viscous dissipation, the irreversible conversion of kinetic energy into internal energy, is represented by the double-dot product $\tau{:}\nabla\mathbf{u}$, which is defined for symmetric $\tau$ as

$$\tau{:}\nabla\mathbf{u} = \tau_{xx}\left(\frac{\partial u}{\partial x}\right) + \tau_{yy}\left(\frac{\partial v}{\partial y}\right) + \tau_{zz}\left(\frac{\partial w}{\partial z}\right) + \tau_{xy}\left(\frac{\partial u}{\partial y} + \frac{\partial v}{\partial x}\right)$$
$$+ \tau_{xz}\left(\frac{\partial u}{\partial z} + \frac{\partial w}{\partial x}\right) + \tau_{yz}\left(\frac{\partial v}{\partial z} + \frac{\partial w}{\partial y}\right) \quad \text{in cartesian coordinates} \tag{51}$$

and

$$\tau{:}\nabla\mathbf{u} = \tau_{rr}\left(\frac{\partial u}{\partial r}\right) + \tau_{\theta\theta}\left(\frac{1}{r}\frac{\partial v}{\partial \theta} + \frac{u}{r}\right) + \tau_{zz}\left(\frac{\partial w}{\partial z}\right) + \tau_{r\theta}\left[r\frac{\partial}{\partial r}\left(\frac{v}{r}\right) + \frac{1}{r}\frac{\partial u}{\partial \theta}\right]$$
$$+ \tau_{z\theta}\left(\frac{1}{r}\frac{\partial w}{\partial \theta} + \frac{\partial v}{\partial z}\right) + \tau_{rz}\left(\frac{\partial u}{\partial z} + \frac{\partial w}{\partial r}\right) \quad \text{in cylindrical coordinates} \tag{52}$$

After dividing out the density, the turbulent kinetic energy, $\kappa$, is substituted into Eq. (47) to compute the turbulent viscosity. It is interesting to note that in the quasi-steady solution, where the production term equals the decay terms because of viscous dissipation, this generalized model reduces to the original algebraic subgrid

scale model of the type used by Smagorinsky (Ref. 12) and Deardorff (Ref. 13 and Ref. 14).

### 2.7.3 $\kappa$–$\varepsilon$ Model

The Navier-Stokes equations may be manipulated to produce exact expressions for $\kappa$, the turbulent kinetic energy, and $\varepsilon$, the rate of dissipation of turbulent kinetic energy (Ref. 15) defined as

$$\varepsilon = \nu \sum_i \sum_j \left( \overline{\frac{\partial u_i}{\partial x_j}} \right)^2 \tag{53}$$

The exact $\kappa$ and $\varepsilon$ equations are modeled by a pair of approximate transport equations developed by Launder and Spalding (Ref. 4) with an extension to treat buoyancy effects. Again, $\kappa^{1/2}$ is the characteristic velocity scale, and the length scale is proportional to $\kappa^{3/2}/\varepsilon$. The transport equation for the product $\rho\kappa$ is given by

$$\frac{d}{dt}\int_{V^*} \rho\kappa \, dV = \int_{S^*} \left[ \rho\kappa(\mathbf{b}-\mathbf{u}) + \left( \frac{\mu}{\sigma_\kappa} \nabla\kappa \right) \right] \cdot \mathbf{n} \, dA$$

$$+ \int_{V^*} \left[ \tau : \nabla\mathbf{u} + \mu\alpha\mathbf{g} \cdot \nabla T - \rho\varepsilon + \kappa S \right] dV \tag{54}$$

where $\alpha$ is the coefficient of thermal expansion. The advection and diffusion of turbulent kinetic energy are given by the terms in the first integral on the right side, and the terms in the second integral represent its production by viscous stresses, production by buoyancy, dissipation, and generation from sources respectively.

The transport equation for the product of the density and the dissipation of the turbulent kinetic energy, $\varepsilon$, is

$$\frac{d}{dt}\int_{V^*} \rho\varepsilon \, dV = \int_{S^*} \left[ \rho\varepsilon(\mathbf{b}-\mathbf{u}) + \left( \frac{\mu}{\sigma_\varepsilon} \nabla\varepsilon \right) \right] \cdot \mathbf{n} \, dA$$

$$+ \int_{V^*} \left[ C_1 \frac{\varepsilon}{\kappa} \tau : \nabla\mathbf{u} + C_1 \frac{\varepsilon}{\kappa} \mu(\alpha\mathbf{g} \cdot \nabla T) - C_2 \rho \frac{\varepsilon^2}{\kappa} + \varepsilon S \right] dV \tag{55}$$

The terms on the right-hand side have meanings analogous to those in Eq. (46). The turbulent viscosity is calculated using the Kolmogorov hypothesis

$$\mu = \frac{C_\mu \rho \kappa^2}{\varepsilon} \tag{56}$$

For this analysis, we assume that the turbulent Prandtl and Schmidt numbers equal unity. Therefore, the turbulent conductivity, $\phi$, is

$$\phi = \mu C_p \tag{57}$$

and the turbulent mass diffusivity, D, is

$$\mathcal{D} = \mu / \rho \tag{58}$$

Both of these transport coefficients are expressed in terms of the turbulent viscosity and thermodynamic properties of the gases.

The values of the five new constants ($C_1$, $C_2$, $C_\mu$, $\sigma_\kappa$, $\sigma_\varepsilon$) appearing in Eqs. (55) and (56) and listed in Table 3 are those suggested by Launder and Spalding (Ref. 4) following an extensive examination of experimental data for free turbulent flows.

**Table 3 Constants used in the $\kappa$–$\varepsilon$ turbulence model**

| $C_1$ | $C_2$ | $C_\mu$ | $\sigma_\kappa$ | $\sigma_\varepsilon$ |
|---|---|---|---|---|
| 1.44 | 1.92 | 0.09 | 1.0 | 1.3 |

### 2.8 Chemical Kinetics

For diffusion flames involving hydrogen (Ref. 16) or hydrocarbon fuels,* we have used a simple one-step global chemical kinetics model that grossly over-simplifies the actual chemical processes. In the present implementation of this model, the only reaction modeled is

$$a(H_2) + b(O_2) + c(N_2) \overset{\omega}{\Rightarrow} d(H_2O) + e(H_2) + f(O_2) + c(N_2) \tag{59}$$

* J. R. Travis and F. R. Krause, "An Analysis of HDR Test T52.14: Diffusion Flames in a Full Scale Nuclear Reactor Containment," Los Alamos National Laboratory report in preparation.

where the coefficients *a*, *b*, *c*, *d*, *e*, and *f* are mole fractions. In modeling nuclear reactor containment buildings, typical computational cell volumes are 1–2 $m^3$; they are larger in some cases. We try to keep cell volumes to about 1 $m^3$ in regions where diffusion flames are expected. For this spatial resolution, there is no attempt to describe flame structure; we simply represent combustion energy release in a complex geometric containment. Furthermore, chemical reaction time scales generally are short compared with fluid motions in these combustion modes, so the many elementary reaction steps and intermediate chemical species can be neglected in this first approximation.

The reaction rate, $\dot{\omega}$, in Eq. (59) is modeled by a modified Arrhenius law. The general expression for the reaction rate is

$$\text{rate}(\text{mole}/\text{m}^3-\text{s}) = C_f[T/T_o]^t[\text{fuel}]^f[\text{oxidizer}]^o e^{-E/\Re T} \tag{60}$$

where $C_f$ is the frequency (or pre-exponential) factor; E is an activation energy; t, f, and o are exponents; fuel and oxidizer indicate local concentrations in $\text{mol}/\text{m}^3$; $\Re$ is the universal gas constant; and $T_o$ is the adiabatic flame temperature. For the $H_2$-$O_2$ reaction, t = 0, f = 1, and o = 1, but in some hydrocarbon simulations, we set t = 1/2 in an attempt to model molecular motion.

The finite-rate chemical kinetics now can be written for the fuel

$$\frac{\partial \rho_F}{\partial t} = -aM_F\dot{\omega} \tag{61}$$

and the oxidizer,

$$\frac{\partial \rho_o}{\partial t} = -bM_o\dot{\omega} \tag{62}$$

where $M_F$ and $M_o$ are the molecular weights of fuel and oxygen, respectively. The chemical energy of combustion is computed as a source for the energy transport equation [Eq. (11)] by

$$Q_c = C_c\dot{\omega} \tag{63}$$

where $C_c = 4.778 \times 10^5$ J/mol ($1.2 \times 10^{12}$ erg/g).

In practice, when solving the finite-rate chemical equations [Eqs. (61) and (62)], we integrate the fuel [Eq. (61)] when the fuel-oxidizer mixture is fuel lean and the oxidizer [Eq. (62)] when the fuel-oxidizer mixture is fuel rich. By using Eq. (59), all components of the combustion process are determined. We have compared the

results of this model with the experimental data for the one-fourth-scale test facility (Ref. 17) and the HDR containment building (Ref. 18) and have found good agreement for the general circulation patterns in complex geometry's, concentrations of combustion products, and temperature distributions throughout the containment buildings.*

## 3 COMPUTATIONAL MODEL

The computational model and solution algorithm for solving the multi-dimensional, time-dependent fluid-flow equations follows the ICEd-ALE methodology first introduced by Hirt et al. (Ref. 19) and used later in other computational fluid dynamics efforts at Los Alamos (Refs. 20–25).

The computational domain is defined by a regular, three-dimensional array of regular parallelepiped cells. First, each coordinate axis is divided into intervals that define cell faces in that direction. The location of each interval is identified by its physical mesh coordinate (x, y, or z in cartesian geometry or r, θ, or z in cylindrical geometry) and a corresponding logical coordinate (i, j, or k) called the mesh index. The domain is divided up in the x-direction by planes passing through the x-direction mesh coordinates and normal to the x-axis. Similarly, sets of planes normal to the other directions divide up space in the y and z directions. The intersections of the three families of planes define a three-dimensional arrangement of cells ("finite volumes"). Figure 2 shows a typical cell along with conventions for identifying faces and vertices.

Values of ρ, I, and p are computed at cell centers, and the face-normal component of velocity is computed at cell faces. Initial values for each variable and appropriate boundary conditions are set at all locations. The continuous integral equations of motion described in Sec. 2 are approximated by finite-volume expressions (discrete algebraic equations) on the computational mesh. Thus, the dynamic state in the problem domain can be approximated by integrating the finite-volume equations in space and time.

In the standard ALE method (Ref. 19), both fluid and grid ($\mathbf{u}_g$) velocities are located at cell vertices. By specifying $\mathbf{u}_g$ to be different from $\mathbf{u}$, the shape and spatial distribution of the mesh may be changed to model a problem with a deformable boundary. Mass, momentum, and energy are exchanged between cells by averaging vertex velocities to produce a cell-face fluxing velocity. Because HMS is designed to compute flows with fixed geometry's, this general mesh motion feature is not needed; therefore, we locate fluid velocities directly on cell faces. Other differences between the standard ALE method and the ALE method implemented in HMS are given in Table 4

* The HDR results are discussed further in the HMS Assessment Document (in preparation).

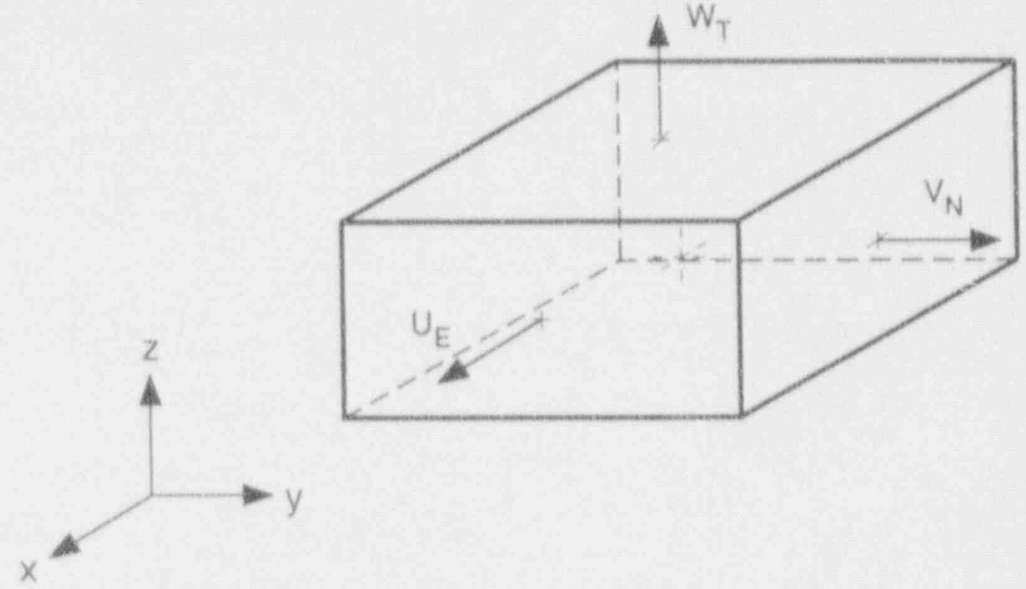


Figure 2 Computational cell. Velocity components are located at face centers: [W] west (-x), [E] east (+x), [S] south (-y), [N] north (+y), [B] bottom (-z), and [T] top (+z); all other variables are located at the cell center.

**Table 4 Comparison of standard ALE and HMS ALE features**

| Standard ICEd-ALE | HMS linearized ICEd-ALE |
|---|---|
| Cell-centered ρ, I, p | Cell-centered ρ, I, p |
| Vertex-centered **u**, momentum | Face-centered **u**, momentum |
| Total energy (E) | Internal energy (I) |
| Pressure work is done only in the implicit Lagrangian phase. | Pressure work is done in both the explicit and implicit Lagrangian phases. |
| Control volumes are (1) computational cells and (2) volumes centered on vertices. | Control volumes are (1) computational cells and (2) volumes centered on cell-faces. |
| Vertex motion algorithm | Vertices stay fixed |
| Arbitrary hexahedral cells | Parallelepiped cells |
| Algorithm for cell volumes | Volume calculations are straightforward |
| Face-fluxing in rezone phase (face fluxing **u** must be computed from vertex **u**) | x-, y-, and z-face fluxing in rezone phase |
| | Linearized volume treatment in implicit Lagrangian phase |

Mesh cells serve as control volumes for cell-centered variables and thus serve as the finite volumes for solving the mass and energy equations. Because velocity components are located at cell faces, a different treatment is needed for the momentum equations. A momentum control volume, $V_m$, is defined as half of each of the two cells sharing a common face (Fig. 3). In this sense, we say that momentum control volumes are "face-centered," although this is strictly true only if both cells are the same size. A momentum control volume for the east face of cell (i, j, k) is $V_m = (V_{i,j,k} + V_{i+1,j,k})/2$ . A similar definition is made for the momentum control volumes that straddle the north and top faces.

Because we are interested only in the Eulerian solution of the flow equations, a full continuous rezone always will be applied (see Sec. 3.3, Rezone Phase), with the Lagrangian phase being only an intermediate step toward the full solution.

Each fluid dynamics time step is broken into three phases as described below and is followed by turbulent transport and heat conduction calculations.

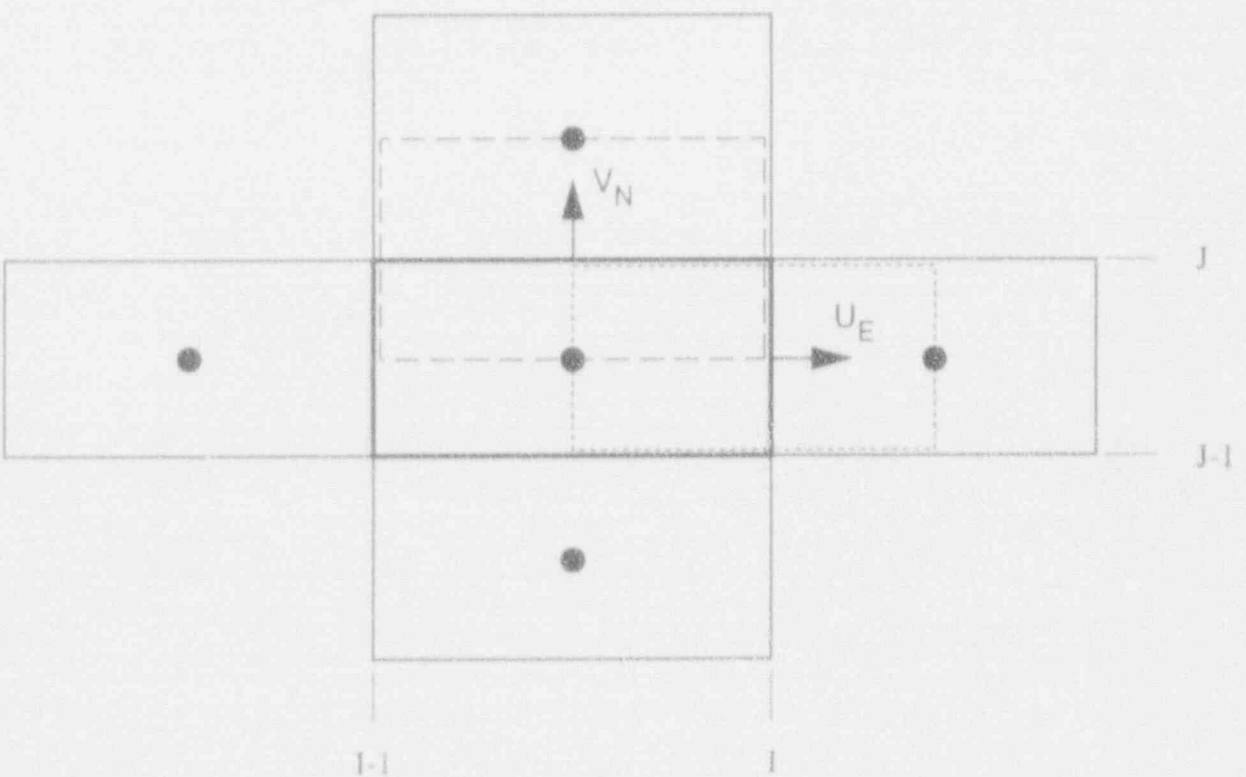


Figure 3 A two-dimensional mesh slice showing the u and v momentum control volumes associated with cell (I, J, K).

### 3.1 Phase A: Explicit Lagrangian Phase

In this phase, the densities, velocities, and specific internal energy fields are updated by the effects of all chemical and physical processes. This includes combustion, condensation, heat transfer, body forces, and turbulence effects.

#### 3.1.1 Condensation Mass and Energy Transfer

Whenever the temperatures of structural surfaces and the adjacent gas differ there will be heat exchange by convection. If condensation occurs, there will be energy and mass transfer from the gas to the condensate—a condensate that typically appears as a thin film. The resulting change in mass and energy of the gas appears as source terms in the Phase A mass and energy equations (Secs. 3.1.4 and 6) and as a heat flux boundary condition in the structural heat conduction solution (Sec. 3.5).

First, we combine Eqs. (29) to (31) to yield an expression for the change in steam density

$$\sum_{HTS} \dot{m}_w = V \frac{\partial \rho_{H_2O}}{\partial t} = - \frac{\Theta_m \sum_{HTS} \left[ \left( \rho_b^A - \rho_s^A \right)_{H_2O} h_w A_w \right]}{\sum_{\alpha} \left( \rho^n c_p \right)} \tag{64}$$

where HTS indicates summation over all of the heat-transfer surfaces in contact with the fluid cell. In terms of the mass condensation source term, $S_\rho$, this becomes

$$S_\rho = \frac{\rho_{H_2O}^A - \rho_{H_2O}^n}{\Delta t} = - \frac{\Theta_m \sum_{HTS} \left[ \left( \rho_b^A - \rho_s^A \right)_{H_2O} h_w A_w \right]}{V \sum_{\alpha} \left( \rho^n c_p \right)} \tag{65}$$

and then solving for $\rho_{H_2O}^A$

$$\rho_{H_2O}^A = \left[ \frac{\rho_{H_2O}^A V \sum_{\alpha} \left( \rho^n c_p \right) + \Delta t \Theta_m \sum_{HTS} \left( \rho_s h_w A_w \right)}{V \sum_{\alpha} \left( \rho^n c_p \right) + \Delta t \Theta_m \sum_{HTS} \left( h_w A_w \right)} \right] \tag{66}$$

Next, for all heat-transfer surfaces, we compute $h_W$ from Eqs (23), (37), (40) and (41) and the corrected heat-transfer coefficient $h_w^*$ from Eqs. (26) to (28). The total energy lost by the gas may be written as

$$\frac{\partial (\rho I)}{\partial t} = \frac{(\rho I)^A - (\rho I)^n}{\Delta t} = \frac{\sum_{HTS} \left[ h_w^* A_w \left( T_w - T_g^A \right) \right]}{V} + S_\rho c_v \left( T_g^A - T_{sat} \right) \tag{67}$$

The terms on the right side of Eq. (67) represent the energy lost by convection and the energy lost in cooling steam from $T_g^A$ to the saturation temperature $T_{sat}$.

Substituting $(\rho c_v T)^A$ for $(\rho I)^A$ and solving for $T_g^A$ gives

$$T_g^A = \frac{(\rho I)^n + \Delta t \left[ \frac{\sum_{HTS} \left( h_w^* A_w \right)}{V} - S_\rho c_v T_{sat} \right]}{(\rho c_v)^A + \Delta t \left[ \frac{\sum_{HTS} \left( h_w^* A_w \right)}{V} - S_\rho c_v \right]} \tag{68}$$

For each wall, the energy exchanged by convection is given by Eq. (22) and the energy exchanged during condensation is

$$q_c = \dot{m}_w \left[ h_{fg} + (c_v)_{liq} \left( T_g^A - T_w \right) \right] \tag{69}$$

### 3.1.2 Hydrogen Combustion

When the relationship between molar quantities $a$ and $b$ for $H_2$ and $O_2$ in Eq. (59) is $a < b/2$, the mixture is fuel lean; the discrete version of Eq. (61) then is used to predict the change in hydrogen density

$$\frac{\rho_{H_2}^A - \rho_{H_2}^n}{\Delta t} = -\left[ a C_f M_{H_2} \left( \frac{\rho_{H_2}^A}{M_{H_2}} \right) \left( \frac{\rho_{O_2}^n}{M_{O_2}} \right) e^{-E/\Re T} \right] \tag{70}$$

an implicit expression for $\rho_{H_2}^A$ where superscripts n and A identify the old time level and Phase A in the new time level. Upon rearrangement, this becomes

$$\Delta\rho_{H_2} \equiv \rho_{H_2}^A - \rho_{H_2}^n = -\rho_{H_2}^n \left\{ 1 - \left[ 1 + \Delta t \, a \, C_f \left( \frac{\rho_{O_2}^n}{M_{O_2}} \right) e^{-E/\Re T} \right]^{-1} \right\} \tag{71}$$

The change in oxygen and water vapor density follow directly from mass conservation and Eq. (59)

$$\Delta\rho_{O_2} \equiv \rho_{O_2}^A - \rho_{O_2}^n = \left( \rho_{H_2}^A - \rho_{H_2}^n \right) M_{O_2} / 2 M_{H_2} \tag{72}$$

and

$$\Delta\rho_{H_2O} \equiv \rho^{A}_{H_2O} - \rho^{B}_{H_2O} = -\left(\rho^{A}_{H_2} - \rho^{B}_{H_2}\right) M_{H_2O} / M_{H_2} \tag{73}$$

If the mixture is fuel rich ($a > b/2$), we first compute the change in oxygen density from the discrete version of Eq. (62)

$$\Delta\rho_{O_2} \equiv \rho^{A}_{O_2} - \rho^{B}_{O_2} = -\rho^{B}_{O_2}\left\{1 - \left[1 + \Delta t\, b\, C_f \left(\frac{\rho^{B}_{H_2}}{M_{H_2}}\right) e^{-E/RT}\right]^{-1}\right\} \tag{74}$$

Then we compute the change in hydrogen density

$$\rho^{A}_{H_2} - \rho^{B}_{H_2} = 2\left(\rho^{A}_{O_2} - \rho^{B}_{O_2}\right) M_{H_2} / M_{O_2} \tag{75}$$

and the change in water vapor density from Eq. (73).

### 3.1.3 Volume Equation

The change in each computational cell volume, $V_c$, is calculated from the discrete approximation to Eq. (8) using the divergence theorem (Appendix A)

$$\frac{V^{A}_{c} - V^{B}_{c}}{\Delta t} = \sum_{f} u^{B}_{f}\, dA_{f} \tag{76}$$

Superscripts A and B denote Lagrangian Phases A and B.

### 3.1.4 Mass Equation

The mass change for each species because of combustion, condensation, and turbulent diffusion is calculated by

$$\frac{\rho^{A}_{c} V^{A}_{c} - \rho^{B}_{\alpha} V^{B}_{c}}{\Delta t} = V^{B}_{c} S^{B}_{\alpha} \tag{77}$$

When comparing Eqs. (9) and (77), we see that

$$S^{B}_{\alpha} = \sum_{f}\left[\rho \mathcal{D} \nabla\left(\frac{\rho_\alpha}{\rho}\right)\right]^{B}_{f} + S_\alpha \tag{78}$$

### 3.1.5 Momentum Equations

The components of the velocity field then can be found from the discrete approximation of Eq. (10)

$$\frac{\rho^{A}\mathbf{u}^{A}V_{s}^{A}-\rho^{n}\mathbf{u}^{n}V_{s}^{n}}{\Delta t}=-V_{m}^{n}\nabla p^{n}+V_{m}^{n}\mathbf{M}^{n}-\sum_{f}\tau_{f}\,dA_{f} \tag{79}$$

where, by comparing with Eq. (10)

$$\mathbf{M}^{n}=\rho g-\mathbf{D} \tag{80}$$

The structural drag vector represents the resistance of internal structures such as pipes, I-beams, catwalks, and such configurations that are impossible to resolve. These internal structures play an important role as heat sinks and, to a lesser degree, as momentum sinks. However, we do attempt to model their momentum effects by

$$\mathbf{D}=\frac{1}{2}\rho C_{D}\,\mathbf{u}|\mathbf{u}|(A/V_{c}) \tag{81}$$

where $(A/V_c)$ represents frontal structural area divided by the fluid volume for every computational cell containing internal structures. Note that A is dependent on the orientation of the structures. For example, there is little resistance to flows parallel to the gratings of the catwalks but quite a different resistance to flows normal to the gratings. The drag coefficient, $C_D$, is determined empirically or selected from tables of drag coefficients of common shapes.

### 3.1.6 Internal Energy Equation

We now can find the change in the total internal energy

$$\frac{\rho^{A}I^{A}V_{c}^{A}-\rho^{n}I^{n}V_{c}^{n}}{\Delta t}=-p^{n}\sum_{f}u_{f}^{n}dA_{f}\;-\;p^{n}\frac{V_{s}^{A}-V_{s}^{n}}{\Delta t}$$

$$+\;\sum_{f}q_{f}^{n}\,dA_{f}\;+\;Q^{n}V_{c}^{n} \tag{82}$$

where $Q^n$ as defined in Eq. (11) contains the energy of combustion, condensation, and heat-transfer effects. The gas-mixture temperature, $T^A$, is computed from a mass-weighted version of Eq. (16)

$$\left(\sum_{\alpha}x_{\alpha}A_{\alpha}\right)\left(T^{A}\right)^{2}+\left(\sum_{\alpha}x_{\alpha}B_{\alpha}\right)\left(T^{A}\right)+\left(\sum_{\alpha}x_{\alpha}C_{\alpha}\right)-I=0 \tag{83}$$

### 3.1.7 Equation of State

Finally, the updated pressure is determined from the equation of state [Eq. (19)]

$$p^A = T^A \sum_\alpha R_\alpha \rho_\alpha^A \tag{84}$$

## 3.2 Phase B: Implicit Pressure Iteration Phase

In this phase, an implicit evaluation of the time-advanced densities, velocities, pressure, and specific internal energy fields is achieved. The purpose of this phase is to compute time-advanced pressures to allow calculations of low-speed (low-Mach-number) flows without any time-step restrictions from the fluid sound speeds. The following argument (Ref. 19) explains the need for this step.

> In an explicit method, pressure forces can be transmitted only one cell each time step, that is, cells exert pressure forces only on neighboring cells. When the time step is chosen so large that sound waves should travel more than one cell, the one cell limitation is clearly inaccurate and a catastrophic instability develops. The instability arises because the explicit pressure gradients lead to excessive cell compressions or expansions when multiplied by too large a time step. This then leads to larger pressure gradients the next cycle, which try to reverse the previous excesses, but since the time step is too large the reversal is also too large and the process repeats itself with a rapidly increasing amplitude. The over response to pressure gradients in this fashion is eliminated by using time-advanced pressure gradients, for then cells cannot compress or expand to the point where gradients are reversed.

In this phase, the mixture equations for cell volume, mass, momentum, and energy are

$$\frac{V_c^B - V_c^A}{\Delta t} = V_c^n \nabla \cdot \left( \mathbf{u}^B - \mathbf{u}^n \right) \tag{85}$$

$$\frac{\rho^B V_c^B - \rho^A V_c^A}{\Delta t} = 0 \tag{86}$$

$$\mathbf{u}^B - \mathbf{u}^A = -\frac{\Delta t}{(\rho V)_m} V_m^n \nabla \left( p^B - p^n \right) \tag{87}$$

and

$$\frac{\rho^B I^B V_c^B - \rho^A I^A V_c^A}{\Delta t} = -V_c^n p^n \nabla \cdot \left( \mathbf{u}^B - \mathbf{u}^n \right) \tag{88}$$

### 3.1.7 Equation of State

Finally, the updated pressure is determined from the equation of state [Eq. (19)]

$$p^A = T^A \sum_\alpha R_\alpha \rho_\alpha^A \tag{84}$$

## 3.2 Phase B: Implicit Pressure Iteration Phase

In this phase, an implicit evaluation of the time-advanced densities, velocities, pressure, and specific internal energy fields is achieved. The purpose of this phase is to compute time-advanced pressures to allow calculations of low-speed (low-Mach-number) flows without any time-step restrictions from the fluid sound speeds. The following argument (Ref. 19) explains the need for this step.

> In an explicit method, pressure forces can be transmitted only one cell each time step, that is, cells exert pressure forces only on neighboring cells. When the time step is chosen so large that sound waves should travel more than one cell, the one cell limitation is clearly inaccurate and a catastrophic instability develops. The instability arises because the explicit pressure gradients lead to excessive cell compressions or expansions when multiplied by too large a time step. This then leads to larger pressure gradients the next cycle, which try to reverse the previous excesses, but since the time step is too large the reversal is also too large and the process repeats itself with a rapidly increasing amplitude. The over response to pressure gradients in this fashion is eliminated by using time-advanced pressure gradients, for then cells cannot compress or expand to the point where gradients are reversed.

In this phase, the mixture equations for cell volume, mass, momentum, and energy are

$$\frac{V_c^B - V_c^A}{\Delta t} = V_c^n \nabla \cdot \left( \mathbf{u}^B - \mathbf{u}^n \right) \tag{85}$$

$$\frac{\rho^B V_c^B - \rho^A V_c^A}{\Delta t} = 0 \tag{86}$$

$$\mathbf{u}^B - \mathbf{u}^A = -\frac{\Delta t}{(\rho V)_m} V_m^n \nabla \left( p^B - p^n \right) \tag{87}$$

and

$$\frac{\rho^B I^B V_c^B - \rho^A I^A V_c^A}{\Delta t} = -V_c^n p^n \nabla \cdot \left( \mathbf{u}^B - \mathbf{u}^n \right) \tag{88}$$

The equation of state for the mixture may be written as

$$\frac{pV}{T\sum_{\alpha} x_{\alpha} R_{\alpha}} = \rho V \tag{89}$$

Equations (85)–(89) are a coupled of set four linear and one nonlinear [Eq. (87)] algebraic equations in five unknowns ($I^B$, $p^B$, $\mathbf{u}^B$, $V^B$, and $\rho^B$). In the following development, we derive an equation for $p^B$ alone. Using Eqs. (85) and (89) we can eliminate $\rho^B$ by rewriting the left side of Eq. (88)

$$\frac{\left(\rho^B I^B V^B\right) - \left(\rho^A I^A V^A\right)}{\Delta t} = \frac{pV\left(I^B - I^A\right)}{\Delta t\, T\sum_{\alpha} x_{\alpha} R_{\alpha}} \tag{90}$$

Multiplying and dividing this last expression by $(T^B - T^A)$ and noting that $(I^B - I^B)/(T^B - T^A) \approx C_v(T^A)$ gives

$$\frac{\left(\rho^B I^B V^B\right) - \left(\rho^A I^A V^A\right)}{\Delta t} = \frac{C_v\left(T^A\right)\left(p^B V^B - p^A V^A\right)}{\Delta t\, T\sum_{\alpha} x_{\alpha} R_{\alpha}} \tag{91}$$

Using this expression for the left side of Eq. (88) and substituting Eq. (85) into the right side of Eq. (88), the energy equation becomes

$$\frac{C_v\left(T^A\right)\left(p^B V^B - p^A V^B + p^A V^B - p^A V^A\right)}{\Delta t\, T\sum_{\alpha} x_{\alpha} R_{\alpha}} = \frac{-\left(V^B - V^A\right)}{\Delta t} p^n \tag{92}$$

where $p^A V^B$ has been added and subtracted from the left side to simplify the algebra. After collecting terms and further rearrangement, this becomes

$$\left(p^B - p^A\right) = -\left\{\left[\sum_{\alpha} x_{\alpha} R_{\alpha} / C_v(T)\right] p^n + p^A\right\}\left(V_c^B - V_c^A\right) / V_c^B \tag{93}$$

This equation can be linearized by rearranging $\left(V_c^B - V_c^A\right) / V_c^B$ and then applying a binomial series to obtain

$$\left(V_c^B - V_c^A\right) / V_c^B \approx \left(V_c^B - V_c^A\right) / V_c^A \tag{94}$$

provided $\left(V_c^B - V_c^*\right) / V_c^A << 1$. Note that this quantity is monitored during a transient simulation to ensure an accurate solution. As the time step decreases, this quantity approaches zero. Next, $V^B$ is eliminated by combining Eqs. (85) and (93), adding and subtracting $p^B$ to the left side, and adding and subtracting $\nabla \cdot \mathbf{u}^A$ on the right side to give

$$\frac{V^A}{\Delta t}\left[\delta p + \left(p^n - p^A\right)\right] = -V^n\{\ \}\left[\nabla \cdot \left(\mathbf{u}^B - \mathbf{u}^A\right) + \nabla \cdot \left(\mathbf{u}^A - \mathbf{u}^n\right)\right] \tag{95}$$

where

$$\{\ \} = \left\{\left[\sum_\alpha x_\alpha R_\alpha / C_v(T)\right] p^n + p^A\right\} \tag{96}$$

and

$$\delta p = p^B - p^n \tag{97}$$

Finally, $\mathbf{u}^B$ is eliminated by substituting the right side of Eq. (87) for $(\mathbf{u}^B - \mathbf{u}^A)$

$$\Delta t^2 V^n \nabla \cdot \left[\frac{V_m^n \nabla \delta p}{(\rho V)_m}\right] - \frac{V^A \delta p}{\{\ \}} = \frac{V^A\left(p^n - p^A\right)}{\{\ \}} + \Delta t\, V^n \nabla \cdot \left(\mathbf{u}^A - \mathbf{u}^n\right) \tag{98}$$

or

$$\Delta t^2 \sum_f \left[\frac{V_m^n \nabla \delta p\, dA}{(\rho V)_m}\right] - \frac{V^A \delta p}{\{\ \}} = \frac{V^A\left(p^n - p^A\right)}{\{\ \}} + \Delta t \sum_f \left(\mathbf{u}^A - \mathbf{u}^n\right)_f dA_f \tag{99}$$

which is second order and linear in $\delta p$. To solve this Poisson-type pressure equation, we use the Preconditioned Conjugate Residual (PCR) method that is described in Appendix B.

This implicit solution of the pressure equation allows for greater efficiency than a purely explicit calculation with reduced time steps. The numerical stability achieved permits pressure waves to traverse more than one computational cell in a time step. In practice, after solving Eq. (99) for $\delta p$, we evaluate $\mathbf{u}^B$ from Eq. (87), $V_c^B$ from Eq. (85), $\rho_\alpha^B$ from

$$\frac{\rho_\alpha^B V_c^B - \rho_\alpha^A V_c^A}{\Delta t} = 0 \tag{100}$$

$p^B$ from Eq. (93), $T^B$ from Eq. (19), and $I^B$ from Eqs. (16) and (17).

### 3.3 Phase C: Rezone Phase

The third phase explicitly performs all the advective flux calculations, repartitioning the dependent variables onto the original mesh. The superscript n+1 (and not C) is used to indicate that this Eulerian rezone phase completes the spatiotemporal integration of the equations of motion from time-level n to time-level n+1. The finite volume equations for mass, momentum, and energy advection, respectively, are as follows

$$\frac{\rho_i^{n+1} V_c^n - \rho_i^B V_c^B}{\Delta t} = -\sum_f \left(\rho^B u^B dA\right)_f \tag{101}$$

$$\frac{\rho^{n+1} \mathbf{u}^{n+1} V_m^n - \rho^B \mathbf{u}^B V_m^B}{\Delta t} = -\sum_f \left(\rho^B \mathbf{u}^B u^B dA\right)_f \tag{102}$$

and

$$\frac{\rho^{n+1} I^{n+1} V_c^n - \rho^B I^B V_c^B}{\Delta t} = -\sum_f \left(\rho^B I^B u^B dA\right)_f \tag{103}$$

Decoupling the rezoning step from the rest of the physics computations facilitates the implementation of different numerical advection algorithms. We have made use of simple donor cell, interpolated donor cell, van Leer (Ref. 26), and FCT (Refs. 27--29) to model the right-hand sides of Eqs. (101)–(103). Phase C is completed by computing $T^{n+1}$ from Eq. (16) and $p^{n+1}$ from Eq. (19).

### 3.4 Turbulence Transport

The final fluid dynamics task in each computational cycle is the explicit updating of turbulence variables.

#### 3.4.1 Algebraic Model

The new time-level turbulent viscosity follows directly from Eq. (47)

$$\mu^{n+1} = C_\mu \rho^{n+1} \left\{ 0.1 \cdot \frac{1}{2} \left[ \left(u^{n+1}\right)^2 + \left(v^{n+1}\right)^2 + \left(w^{n+1}\right)^2 \right] \right\}^{1/2} \tag{104}$$

#### 3.4.2 Subgrid Scale Model

The product $\rho\kappa$ is updated with a discrete version of Eq. (50)

$$\frac{(\rho\kappa)^{n+1}V_c^n - (\rho\kappa)^n V_c^n}{\Delta t} = \sum_f \left[\left\{-(\rho\kappa)^n u^{n+1} + \mu^n \nabla\kappa^n\right\} dA\right]_f \tag{105}$$

$$-\frac{2}{3}(\rho\kappa)^n \sum_f \left[u^{n+1} dA\right]_f + (\tau:u)^{n+1} V_c^n - \frac{\rho^n (\kappa^n)^{3/2}}{\ell} V_c^n$$

The new time-level turbulent viscosity, $\mu^{n+1}$, then is computed from Eq. (104).

### 3.4.3 $\kappa \cdot \varepsilon$ Model

The new time-level products $\rho\kappa$ and $\rho\varepsilon$ are computed from the discrete versions of Eqs. (54) and (55)

$$\frac{(\rho\kappa)^{n+1}V_c^n - (\rho\kappa)^n V_c^n}{\Delta t} = \sum_f \left[\left\{-(\rho\kappa)^n u^{n+1} + \frac{\mu^n}{\sigma_\kappa}\nabla\kappa^n\right\} dA\right]_f \tag{106}$$

$$+ (\tau:u)^{n+1} V_c^n + \mu^n \left(\alpha^n g \cdot \nabla T^n\right) V_c^n - (\rho\varepsilon)^n V_c^n + \kappa^n S^n V_c^n$$

and

$$\frac{(\rho\varepsilon)^{n+1}V_c^n - (\rho\varepsilon)^n V_c^n}{\Delta t} = \sum_f \left[\left\{-(\rho\varepsilon)^n u^{n+1} + \frac{\mu^n}{\sigma_\varepsilon}\nabla\varepsilon^n\right\} dA\right]_f \tag{107}$$

$$+ C_1 \frac{\varepsilon^n}{\kappa^n}(\tau:u)^{n+1} V_c^n + C_1 \frac{\varepsilon^n}{\kappa^n}\mu^n \left(a^n g \cdot \nabla T^n\right) V_c^n - C_2 \frac{\rho^n (\varepsilon^n)^2}{\kappa^n} V_c^n + \varepsilon^n S^n V_c^n$$

The turbulent viscosity then is computed from Eq. (56)

$$\mu^{n+1} = \frac{C_\mu \rho^{n+1} (\kappa^{n+1})^2}{\varepsilon^{n+1}} \tag{108}$$

The new time step is controlled by checking the entire computational mesh for a material velocity Courant condition and a diffusion stability limit condition.

## 3.5 Heat Conduction through Structures

Heat transfer through structural components (usually concrete and steel) is modeled as one-dimensional heat conduction. The structure is represented numerically by N finite-difference nodes spaced $\delta x$ apart; node number 1 is on the structure-gas

boundary (Fig. 4). New time-level temperatures at all but the first and last nodes are computed from an implicit finite-difference approximation to Eq. (35)

$$\frac{T_i^{n+1} - T_i^n}{\Delta t} = \frac{k}{\rho c_p} \frac{T_{i-1}^{n+1} - 2T_i^{n+1} + T_{i+1}^{n+1}}{\delta x^2}, \quad 2 \le i \le N-1 \tag{109}$$

Collecting coefficients of like T terms, Eq. (109) becomes

$$\Lambda T_{i-1}^{n+1} - (1+2\Lambda) T_i^{n+1} + \Lambda T_{i+1}^{n+1} = -T_i^n \tag{110}$$

A corresponding expression at the gas-structure interface for node 1 is

$$-\left(\tfrac{1}{2} + \eta h_w + \Lambda\right) T_1^{n+1} + \Lambda T_2^{n+1} = -\tfrac{1}{2} T_1^n - \eta\left(q_c - \sum q_r + q_{wr} + h_w T_g^{\Lambda}\right) \tag{111}$$

where

$$\Lambda \equiv \frac{k \Delta t}{\rho c_p \delta x^2} \tag{112}$$

$$\eta \equiv \frac{\Delta t}{\rho c_p \delta x} \tag{113}$$

and k, $\rho$, and $c_p$ are the conductivity, density, and specific heat of the structure material.

Equations (110), (111), and a boundary-condition-dependent equation for node N are a linear system of N equations for the unknown temperatures $T_i^{n+1}$ that are found from a tridiagonal matrix solution algorithm.

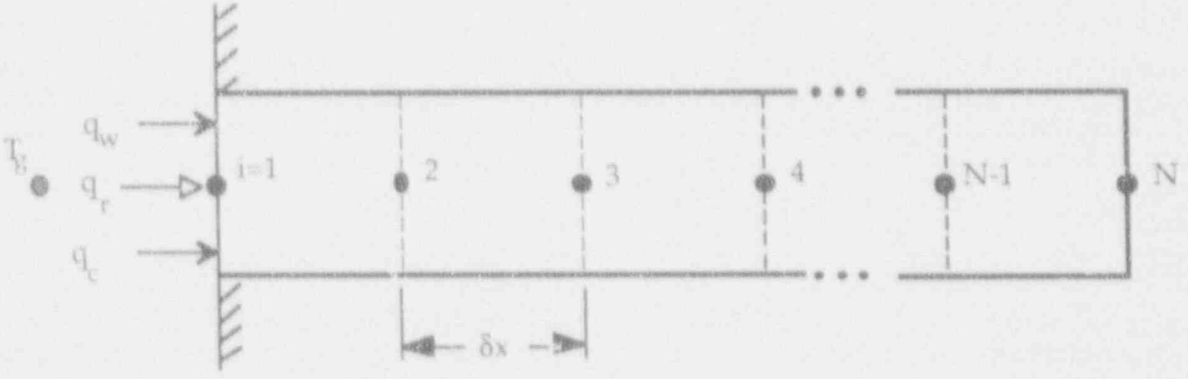


Figure 4 Geometry for one-dimensional heat conduction.

# 4 SUMMARY

In this report we have described the theory behind the HMS computer code and the computational model used to numerically integrate the governing equations in time and space.

The core of the code is based on the conservation laws for mass, momentum, and energy, which were presented in integral form to more closely mirror the finite volume formulation for the discrete equations. The basic fluid dynamics equations are supplemented with relations for multiple gas species, heat transfer, condensation, turbulence transport, and a simple finite-rate global chemical kinetics model for combustion.

An ICEd-ALE numerical method, adapted to fixed geometry, is used to solve the equations of motion. Each time step is split into three phases: (1) an explicit Lagrangian phase where most of the physics is done, (2) an implicit Lagrangian phase where time-advanced pressure, velocity, density, and energy are computed together, and (3) a rezone phase where problem variables are repartitioned onto the original mesh. Turbulence quantities and structural temperatures then are advanced to complete the time step.

Using the above field equation model coupled with finite-rate global chemical kinetics, we have successfully analyzed the hydrogen and hydrocarbon diffusion flames occurring in a nuclear reactor containment under accident conditions. These combustion modes are the easiest to model and analyze when compared with other modes of combustion, such as propagating flames in premixed fuel/oxidizer volumes. Deflagrations, flame acceleration and transition from deflagration to detonation (DDT), and detonations are all important combustion modes that have not been modeled successfully in complex reactor containment structures. We will address some of these issues and recommend approaches for solutions in Sec. 5.

# 5 RESEARCH DIRECTIONS

## 5.1 Nonreactor Combustion Modeling

The basic framework necessary for modeling combustion phenomena associated with nonreactor systems has been established. However, research in several areas is needed, including radioactive and nonradioactive combustion characteristics, material transport model improvement, lumped-parameter and field model coupling, development of system safeguards models, and experimental validation and verification of system (network) modeling codes.

Very little is known about how radioactive materials burn, particularly how they may combine with nonradioactive burning material. Currently, highly empirical data are being used to determine the airborne fraction of radioactive release from

contaminated materials. Research needs to be performed to develop better models using a larger experimental data base.

The transport of smoke with its radioactive component is perhaps the single most important aspect of nuclear materials fires. Models that accurately simulate the behavior of particulate and gaseous materials as they move through the nuclear facility are needed. In particular, interparticle dynamics and particle depletion models need to be developed and refined.

For large volumes in nonreactor systems (such as large rooms) the lumped-parameter approach is not suitable. In this case, a multidimensional model is needed and can be coupled with a lumped-parameter ventilation network. This capability currently does not exist, and research needs to be devoted to establishing this capability.

Research directions toward developing system safeguards models also need to be pursued. These models would simulate the effect of sprinklers, halon discharge, and demisters. The adequacy of a fire protection system can be evaluated with these models.

Finally, the lumped-parameter codes and models need to be validated through experiments. Large systems of interconnected ductwork, rooms, filters, dampers, and fans need to be included in the experimental system. This experimental system, with proper instrumentation for measuring temperatures, pressures, flows, and aerosol concentrations, would be invaluable for obtaining experimental data.

### 5.2 Reactor Combustion Modeling

The field equation approach has been applied successfully to diffusion flame combustion modes in complex reactor containment geometries. To evaluate other major concerns involving combustion phenomena during a severe accident in a reactor containment, we must develop modeling capabilities to investigate flame propagation in premixed, complex, multidimensional volumes. This includes laminar and turbulent deflagrations, flame acceleration and DDTs, and detonations. We also wish to model radioactive and nonradioactive aerosol dynamics and the interaction of the nonoxidized and oxidized aerosols with the propagating flame. Accident mitigation concepts such as water sprays and their influence on a steam-air-hydrogen environment must be assessed. All of these phenomena must be evaluated in terms of thermal and mechanical loads on the containment and on safety-related equipment. Some of these research areas include adaptive gridding, detailed chemical kinetics, turbulence, radiation heat transfer, aerosol dynamics, and model validation with experimental data.

For flames propagating through complex geometries; spatial resolution of the combustion process and the flame front are important. This will require dynamic

implementation of adaptive gridding algorithms (Ref. 30) to resolve the flame front sufficiently as it propagates through the containment.

Global finite-rate chemical kinetics, which were used for diffusion flame analysis, will not be adequate for modeling propagating flames. For the wide range of conditions (pressure, temperature, and gas composition) likely to be found in reactor containments, it will be necessary to couple the fluid dynamics with a detailed chemical kinetics reaction set as suggested by Oran et al (Ref. 31). The disadvantage of directly coupling chemical kinetics with 48 reactions and 9 species is that for large time-dependent, three-dimensional problems, the solution algorithm is currently computationally prohibitive. An alternative approach (Refs. 32 and 33) could be to solve the detailed chemical kinetics for the expected range of pressures, temperatures, and gas compositions. From these conditions and solutions, we can determine an induction time, a reaction time, and the amount of chemical energy released. These parameters could be approximated with analytic functions or tabulated in a parameter space table. A modified-combustion-parameter, P, transport equation can be written as

$$\frac{\partial P}{\partial t} + u \cdot \nabla P = \nabla(\Theta \nabla P) + \frac{1}{\tau_i(T, P, x_i)} \tag{114}$$

where $\tau_i$ and $\Theta$ represent the induction time and turbulent transport coefficient, respectively. Initially, $P \equiv 0$, so that when $P \geq 1$, the induction time has elapsed and the chemical energy of combustion is released over a period of time equal to the reaction time, $\tau_R$. In this way, an approximate method for coupling the fluid dynamics and detailed chemical kinetics can be achieved. The disadvantage of this procedure is that fluid dynamics effects like acoustic waves and turbulence intensities would not actually influence the individual chemical reaction rates and therefore the reaction time. It may be possible to add an additional variable to the parameter space table to account for turbulence and the influence that turbulence has on the reaction rates, induction time, and reaction time. If the reaction rates could be correlated to the intensity or kinetic energy of the local turbulent conditions, then the first term on the right-hand side of Eq. (114), the turbulent diffusion of P, could be eliminated from the equation.

For diffusion flame modeling, we have found that turbulent buoyant plumes generally are represented adequately with the two-equation $\kappa$ - $\varepsilon$ model. However, Zyvoloski* has shown that the most accurate plume dynamic predictions are provided with the three-equation $\kappa$ - $\varepsilon$ - $T'^2$ model. For this model, the additional transport equation for the average temperature fluctuations squared is solved. Reynolds stresses and turbulent energy fluxes then are calculated and used directly in the Reynolds-averaged Navier-Stokes equations. At this point, it is not clear

* G. Zyvoloski, "Simulations of Intense Fires: A Comparison of Turbulence Models," Los Alamos National Laboratory report in preparation.

whether this three-equation model is needed to describe diffusion flame plume dynamics. If the survival and proper functioning of safety-related equipment located near diffusion flames remains an unresolved safety issue, then it may be necessary to use a three-equation model. Also, if the diffusion flame plume impinges on the steel shell liner, a higher temperature can be predicted than what actually is observed. Although this result is conservative, there is actually more entrainment of cooler material into the plume than predicted. It may be necessary for "best-estimate" calculations of thermal loads on the containment shell to use the three-equation model.

Radiation heat transfer from diffusion and propagating flames can be of major importance. For example, in optically thick regions near hydrocarbon diffusion flames, the coupling between carbon or soot, the fluid field, and the radiation field will be strong, whereas in optically thin regions far from the flame, this coupling will be weak. To include these effects, we consider adopting an extension of a nonequilibrium radiation model originally developed by Alme, Westmoreland, and Fry (Ref. 34) and then extended by Daly (Ref. 35). In this model, the local energy densities of the radiation field, the fluid, and the particles can be different. Because the speed of light is inherent in these equations, any practical solutions must be obtained from an implicit finite-difference form of the equations.

Water sprays and aerosol dynamics are similar problems. For example, in a steam-air-hydrogen environment, the spray water droplets and aerosol particles provide condensation nuclei to reduce the steam concentration in the mixture. Two undesired physical effects occur: (1) hydrogen concentrations increase as the steam condenses and (2) turbulence levels increase with condensation and droplet and particle momentum exchange with the continuous gas phase. Nonoxidized aerosols in the presence of hydrogen combustion could increase the energy release as aerosols contribute to the combustion process. On the other hand, water sprays such as mists can be huge energy sinks and provide mitigation methods for suppressing or controlling potentially damaging combustion modes. These trade-offs must be evaluated and assessed to provide input for severe accident management policies.

These modeling questions and the coupled phenomena are difficult, and the physical geometry to which they must be applied is so complex that model and code verification is essential. This can be accomplished only with modelers and experimenters working very closely in a collaborative effort to resolve and understand the relevant phenomena. Separate-effect experiments must be performed to validate individual physical and chemical processes wherever possible. Integrated tests at several scales will provide data and the confidence for computer models to be used to extrapolate to full-scale geometry's. Only in this way can numerical modeling and simulations address the issues and answer the questions concerning the problems involved in nuclear reactor safety.

## REFERENCES


1. G. K. Batchelor, *An Introduction to Fluid Dynamics* (Cambridge University Press, Cambridge, 1967).

2. P. A. Thompson, *Compressible-Fluid Dynamics* (McGraw-Hill Book Co., New York, 1972).

3. S. Gordon and B. J. McBride, "Computer Program for Calculation of Complex Chemical Equilibrium Compositions, Rocket Performance, Incident and Reflected Shocks, and Chapman-Jouget Detonations," NASA Special Publication SP-273 (1971).

4. B. E. Launder and D. B. Spalding, "The Numerical Computation of Turbulent Flows," Comp. Meth. Appl. Mech. Eng. **3**, 269 (1974).

5. R. B. Bird, W. E. Stewart, and E. N. Lightfoot, *Transport Phenomena* (John Wiley and Sons, New York, 1960).

6. W. M. Rohsenow and H. Choi, *Heat, Mass, and Momentum Transfer* (Prentice-Hall, Englewood Cliffs, New Jersey, 1961).

7. J. R. Travis, "Hydrogen Diffusion Flames in a MARK III Containment," Joint ANS/ASME Conf. on Design, Construction, and Operation of Nuclear Power Plants, Portland, OR (1984).

8. H. Schlicting, *Boundary-Layer Theory*, (McGraw-Hill, New York, 1968).

9. R. S. Brodkey, *The Phenomena of Fluid Motions* (Addison Wesley, Boston, 1969).

10. T. Cebeci and A. M. O. Smith, *Analysis of Turbulent Boundary Layers* (Academic Press, New York, 1974).

11. W. Rodi, *Turbulence Models and Their Application in Hydraulics* (International Association for Hydraulic Research, Delft, The Netherlands, 1980).

12. J. Smagorinsky, "General Circulation Experiments with the Primitive Equations," Monthly Weather Rev. **91**, 99 (1963).

13. J. W. Deardorff, "A Numerical Study of Three-Dimensional Turbulent Channel Flow at Large Reynolds Numbers," J. Fluid Mech. **41**, 453 (1970).

14. J. W. Deardorff, "On the Magnitude of the Subgrid Scale Eddy Coefficient," J. Comput. Phys. **7**, 120 (1971).

15. P. Bradshaw, T. Cebeci, and J. H. Whitelaw, *Engineering Calculation Methods in Turbulent Flow* (Academic Press, New York, 1981).

16. J. R. Travis, "A Heat, Mass, and Momentum Transport Model for Hydrogen Diffusion Flames in Nuclear Reactor Containments," Nuclear Engr. Des. **101**, 149 (1987).

17. F. Tamanini, E. A. Ural, and J. L. Chaffee, "Hydrogen Combustion Experiments in a 1/4-scale Model of a MARK III Nuclear Reactor Containment," Factory Mutual Corporation Interim report Y101-1 (May 1987).

18. L. Valencia, "Brandschutzversuche im Containment HDR-Versuchsgruppe BRA Versuche T52.1/T52.2" ("Fire Protection Tests in the Containment HDR-Test Group BRA Tests T52.1/T52.2"), Kernforschungszentrum Karlsruhe report PHDR-Arbeitsbericht Nr. 5 075/86 (February 1987).

19. C. W. Hirt, A. A. Amsden, and J. L. Cook, "An Arbitrary Lagrangian-Eulerian Computing Method for All Flow Speeds," J. Comp. Phys. **14**, 227 (1974).

20. A. A. Amsden and C. W. Hirt, "YAQUI: An Arbitrary Lagrangian-Eulerian Computer Program for Fluid Flow at All Speeds," Los Alamos Scientific Laboratory report LA-5100 (March 1973).

21. J. D. Ramshaw and J. K. Dukowicz, "APACHE: A Generalized-Mesh Eulerian Computer Code for Multicomponent Chemically Reactive Fluid Flow," Los Alamos Scientific Laboratory report LA-7427 (January 1979).

22. A. A. Amsden, H. M. Ruppel, and C. W. Hirt, "SALE: A Simplified ALE Computer Program for Fluid Flow at All Speeds," Los Alamos Scientific Laboratory report LA-8095 (June 1980).

23. L. D. Cloutman, J. K. Dukowicz, J. D. Ramshaw, and A. A. Amsden, "CONCHAS-SPRAY: A Computer Code for Reactive Flows with Fuel Sprays," Los Alamos National Laboratory report LA-9294-MS (May 1982).

24. A. A. Amsden, J. D. Ramshaw, P. J. O'Rourke, and J. K. Dukowicz, "KIVA: A Computer Program for Two- and Three-Dimensional Fluid Flows with Chemical Reactions and Fuel Sprays," Los Alamos National Laboratory report LA-10245-MS (February 1985).

25. A. A. Amsden, P. J. O'Rourke, and T. D. Butler, "KIVA-II: A Computer Program for Chemically Reactive Flows with Sprays," Los Alamos National Laboratory report LA-11560-MS (May 1989).

26. B. Van Leer, "Towards the Ultimate Conservation Difference Scheme V. A Second-Order Sequel to Godunov's Method," J. Comp. Phys. **32**, 101 (1979).

27. J. P. Boris and D. L. Book, "Solution of the Continuity Equation by the Method of Flux-Corrected Transport," Meth. in Comp. Phys. **16**, 85 (1976).

28. S. T. Zalesak, "Fully Multidimensional Flux-Corrected Transport Algorithms for Fluids," J. Comp. Phys. **31**, 335 (1979).

29. M. R. Baer and R. J. Gross, "A Two-Dimensional Flux Corrected Transport Solver for Convectively Dominated Flows," Sandia National Laboratories report SAND 85-0163 (1986).

30. E. S. Oran and J. P. Boris, *Numerical Simulation of Reactive Flow* (Elsevier, New York, 1987).

31. E. S. Oran, T. R. Young, J. P. Boris, and A. Cohen, "Weak and Strong Ignition. I. Numerical Simulations of Shock Tube Experiments," Combustion and Flame **48**, 135 (1982).

32. E. S. Oran and J. P. Boris, "Weak and Strong Ignition. II. Sensitivity of the Hydrogen-Oxygen System," Combustion and Flame **48**, 149 (1982).

33. E. S. Oran, J. P. Boris, T. R. Young M. Flanigan, M. Picone, and T. Burks, "Simulations of Gas Phase Detonations: Introduction of an Induction Parameter Model," Naval Research Laboratory memorandum report 4255 (June 1980).

34. M. L. Alme, C. Westmoreland, and M. A. Fry, "Non-Equilibrium Radiation for the HULL Code," Air Force Weapons Laboratory report AFWL TR-76-244 (1976).

35. B. J. Daly, "Modifications of the CONCHAS-SPRAY Code for Entrained Flow Gasification Studies, Final Report 5/1/84-12/31/85," Los Alamos National Laboratory report LA-10754-MS (June 1986).

36. T. M. Apostol, *Mathematical Analysis: A Modern Approach to Advanced Calculus* (Addison-Wesley, Boston, 1957).

37. G. H. Golub and C. F. Van Loan, *Matrix Computations* (The Johns Hopkins University Press, Baltimore, 1983).

38. R. Chandra, "Conjugate Gradient Methods for Partial Differential Equations," Ph.D. Thesis, Yale University (1978).

39. T. Dupont, R. P. Kendall, and H. H. Rachford Jr., "An Approximate Factorization Procedure for Solving Self-Adjoint Elliptic Difference Equations," SIAM J. Numer. Anal. **5**, 559 (1968).

# APPENDIX A
# GAUSS' DIVERGENCE THEOREM

The divergence of a continuously differentiable vector $\Phi$ integrated over a finite volume V may be written as

$$\int_V \nabla \cdot \Phi \, dV$$

Using Gauss' Divergence Theorem, this may be expressed as a surface integral

$$\int_V \nabla \cdot \Phi \, dV = \int_S \Phi \cdot n \, dA \qquad \text{(A-1)}$$

A rigorous development of Eq. (A-1) may be found in most advanced calculus texts; for example, see Apostol (1967).

A discrete approximation to the surface integral, which is applied to hexahedral control volumes, is obtained by summing the individual contributions from each face, f

$$\int_S \Phi \cdot n \, dA \approx \sum_f \Phi_f \, dA_f \qquad \text{(A-2)}$$

where $\Phi_f$ is the outward face-normal component of $\Phi$ and $dA_f$ is the face area. For the regular parallelepiped cells used in HMS, the sum is over the west, east, south, north, bottom, and top faces (abbreviated as W, E, S, N, B, and T respectively).

# APPENDIX B
# PRECONDITIONED CONJUGATE RESIDUAL ALGORITHM

## 1 INTRODUCTION

The pressure equation [Eq. (103), Sec. 3.2] is solved by the preconditioned conjugate residual (PCR) method described in this section. Consider the linear system

$$\mathbf{A}\mathbf{z} = \mathbf{b} \tag{B-1}$$

where A is an n by n symmetric positive definite (SPD) matrix, $\mathbf{z}$ is a solution vector, and $\mathbf{b}$ is known. The residual vector $\mathbf{r} \equiv \mathbf{b} - \mathbf{A}\mathbf{x}$, a measure of error of any vector $\mathbf{x}$ from the exact solution given in Eq. (B-1), is the focus of the development that follows. Variable definitions that are applicable only in this appendix are listed in Sec. 2.

## 2 DEFINITION OF VARIABLES

| | |
|---|---|
| A | n-by-n SPD coefficient matrix |
| $\mathbf{b}$ | Right-hand side vector |
| B | Diagonal of matrix A |
| D | Diagonal of matrix M |
| k | Iteration count |
| L | Strictly lower triangular part of A |
| M | n-by-n SPD preconditioning matrix |
| n | Number of equations to be solved |
| $\mathbf{p}$ | Search vector |
| Q | Nonsingular matrix such that $M = QQ^T$ |
| $\mathbf{q}$ | Working array |
| $\hat{\mathbf{r}}$ | Residual vector for preconditioned system |
| $\mathbf{r}$ | Residual vector ( $\mathbf{r} \equiv \mathbf{b} - \mathbf{A}\mathbf{x}$ ) |
| U | Strictly upper triangular part of A |
| V | Cell volume |
| $\mathbf{x}$ | Solution vector estimate |
| $\mathbf{z}$ | Solution vector for $\mathbf{A}\mathbf{z} = \mathbf{b}$ |
| $\alpha_k$ | Step length |
| $\beta_k$ | Orthogonalization coefficient |
| $\varepsilon$ | Global convergence criteria |
| $\lambda$ | Eigenvalue |

## 3 MOTIVATION

The guiding philosophy behind the PCR method can be shown by first considering the functional $E_\mu(\mathbf{x})$ defined as

$$E_\mu(\mathbf{x}) \equiv \tfrac{1}{2}( (\mathbf{x}-\mathbf{z}), A^\mu(\mathbf{x}-\mathbf{z}) ) \tag{B-2}$$

where $( \cdot , \cdot )$ denotes an inner product, for example, $(\mathbf{x}, A\mathbf{x}) \equiv \mathbf{x}^T A\mathbf{x}$. $E_\mu(\mathbf{x})$ is defined as the error functional and is equal to one-half the square of the $A^\mu$ norm of $(\mathbf{x} - \mathbf{z})$. The exponent $\mu$ takes on positive integer values; $\mu = 1$ for conjugate gradient minimization, and $\mu = 2$ for conjugate residual minimization (the choice made here). Recalling $\mathbf{r} = \mathbf{b} - A\mathbf{x} = -A(\mathbf{x} - \mathbf{z})$, we write $E_2(\mathbf{x})$ as

$$E_2(\mathbf{x}) \equiv \tfrac{1}{2}( A(\mathbf{x}-\mathbf{z}), A(\mathbf{x}-\mathbf{z}) ) = \tfrac{1}{2}( \mathbf{r}, \mathbf{r} ) \tag{B-3}$$

It follows that the minimum of $E(\mathbf{x})$ as $\mathbf{x}$ varies over $\mathbf{R}^n$ is

$$\frac{\partial E_2(\mathbf{x})}{\partial \mathbf{x}} \equiv A(A\mathbf{x} - \mathbf{b}) = -A\mathbf{r} \tag{B-4}$$

Hence, the problem of minimizing the quadratic error functional $E_2(\mathbf{x})$ is seen to be equivalent to solving the original linear system [Eq. (B-1)] with the solution being $\mathbf{x} = \mathbf{z}$ in each case.

The goal of the PCR procedure is to successively calculate improved estimates for the solution vector $\mathbf{x}_k$

$$\mathbf{x}_k = \mathbf{x}_{k-1} + \alpha_k \mathbf{p}_k \tag{B-5}$$

by minimizing $E(\mathbf{x})$ along yet-to-be-determined search directions, $\mathbf{p}_k$, where $\alpha_k$ and $\beta_k$, are constants. Substituting Eq. (B-5) into Eq. (B-3) gives

$$E_2(\mathbf{x}_k) \equiv \tfrac{1}{2}( A(\mathbf{x}_{k-1} + \alpha_k \mathbf{p}_k - \mathbf{z}), A(\mathbf{x}_{k-1} + \alpha_k \mathbf{p}_k - \mathbf{z}) ) \tag{B-6}$$

The optimum value of $\alpha_k$ minimizes $E_2(\mathbf{x})$ with respect to $\alpha_k$

$$\frac{\partial E_2(\mathbf{x}_k)}{\partial \alpha_k} = \alpha_k ( A\mathbf{p}_k, A\mathbf{p}_k ) - ( \mathbf{r}_{k-1}, A\mathbf{p}_k ) = 0 \tag{B-7}$$

or

$$\alpha_k = ( \mathbf{r}_{k-1}, A\mathbf{p}_k ) / ( A\mathbf{p}_k, A\mathbf{p}_k ) \tag{B-8}$$

Because constant values of $E(\mathbf{x})$ correspond to level surfaces (hyperellipsoids) in $R^n$, it is natural to select the negative gradient of $E(\mathbf{x})$ [Eq. (B-3)] as the search direction, with $\nabla E(\mathbf{x}_k)$ being the direction of most rapid change at $\mathbf{x}$. This is equivalent to using $\mathbf{r}$ as the search direction vector $\mathbf{p}$ in Eq. (B-5) and is known as the method of steepest descent. The set of residual vectors $\mathbf{r}_i$ $(i = 0,k)$ in the steepest descent method is not usually linearly independent, and if the condition number of A, $\kappa(A) = \lambda_{max}/\lambda_{min}$, is large (corresponding to highly elongated ellipsoids), the convergence can be slow. Instead, we compute $\mathbf{p}_k$

$$\mathbf{p}_k = \mathbf{r}_{k-1} + \beta_k \mathbf{p}_{k-1} \tag{B-9}$$

subject to the requirement

$$(\mathbf{p}_i, A\mathbf{p}_j) = 0 \text{ for } i \neq j \leq n \tag{B-10}$$

Computed this way, the search directions, $\mathbf{p}_i$, are A-*conjugate* (or A-orthogonal) to all other directions $\mathbf{p}_j$, and the solution vector $\mathbf{x}_k$ computed from Eq. (B-5) will minimize $E_2(\mathbf{x}_k)$ over the span $\{\mathbf{p}_0, \mathbf{p}_1, \ldots \mathbf{p}_k\}$ (Ref. 37). Chandra (Ref. 38) shows that the family of conjugate direction methods (which includes the conjugate residual method) are optimal among all linear iterative methods with respect to $E_\mu(\mathbf{x})$.

The orthogonalization coefficient $\beta_k$ is found by substituting Eq. (B-9) into Eq. (B-10)

$$\beta_k = -(\mathbf{r}_{k-1}, A\mathbf{p}_{k-1})/(\mathbf{p}_{k-1}, A\mathbf{p}_{k-1}) \tag{B-11}$$

## 4 PRECONDITIONING

The solution to Eq. (B-1) can be obtained more rapidly if we precondition the system $A\mathbf{x} = \mathbf{b}$. Instead, we solve

$$A'\mathbf{x}' = \mathbf{b}' \tag{B-12}$$

where, $A' = Q^{-1}AQ^{-T}$, $\mathbf{x}' = Q^T\mathbf{x}$, $\mathbf{b}' = Q^{-1}\mathbf{b}$, and Q is a nonsingular matrix. If $Q^{-1}AQ^{-T} = I$, then $\kappa(A')$ is small and $A' \approx Q^{-1}Q^{-T}$. Defining $M \equiv Q^{-1}Q^{-T}$, as the preconditioning matrix, we use the factorization of Dupont, Kendall, and Rachford (Ref. 39) for M

$$M = (L + D)D^{-1}(D + U) \tag{B-13}$$

to solve a system of the form $M\mathbf{u} = \mathbf{v}$, which may be inverted rapidly by an LU decomposition. The additional effort required to solve for $\mathbf{u}$ is more than offset by the faster convergence of the PCR algorithm presented in the next section.

## 5 THE NUMERICAL PCR ALGORITHM

The solution to the linear system [Eq. (B-1)] is obtained from the following version of the PCR method and closely follows the algorithm of Chandra (Ref. 37) (Sec. 5.4).

**Step 1. Initialization**

Choose $\mathbf{x}_0$ (B-14a)

$\mathbf{r}_0 = \mathbf{b} - A\mathbf{x}_0$ (B-14b)

**Solve:** $M\hat{\mathbf{r}}_0 = \mathbf{r}_0$ for $\hat{\mathbf{r}}_0$ (B-14c)

$\mathbf{p}_0 = \hat{\mathbf{r}}_0$ (B-14d)

If $[\, r_0/V \,]_m < \varepsilon$ for $1 \le m \le n$, quit (solution is already converged). (B-14e)

$q_0 = 0$ (B-14f)

**Step 2. Compute new search, solution, and residual vectors**

For $k = 1, 2, \ldots, n$

$\beta_k = -(\hat{\mathbf{r}}_{k-1}, \mathbf{q}_{k-1}) / (\mathbf{q}_{k-1}, A\mathbf{p}_{k-1})$ (B-15a)

$\mathbf{p}_k = \hat{\mathbf{r}}_{k-1} + \beta_k \mathbf{p}_{k-1}$ (B-15b)

**Solve:** $M\mathbf{q}_k = A\mathbf{p}_k$ for $\mathbf{q}_k$ (B-15c)

$\alpha_k = (\hat{\mathbf{r}}_{k-1}, A\mathbf{r}_{k-1}) / (\mathbf{q}_k, A\mathbf{p}_k)$ (B-15d)

$\mathbf{x}_k = \mathbf{x}_{k-1} + \alpha_k \mathbf{p}_k$ (B-15e)

$\hat{\mathbf{r}}_k = \hat{\mathbf{r}}_{k-1} - \alpha_k \mathbf{q}_k$ (B-15f)

**Step 3. Has solution converged?**

$\mathbf{r}_k = \mathbf{r}_{k-1} - \alpha_k A\mathbf{p}_k$ (B-16a)

If $[r_k / V]_m < \varepsilon$ for $1 \le m \le n$, quit; otherwise go to step 2. (B-16b)

NRC FORM 335 (2-89) NRCM 1102, 3201, 3202 — U.S. NUCLEAR REGULATORY COMMISSION

# BIBLIOGRAPHIC DATA SHEET

1. REPORT NUMBER (Assigned by NRC, Add Vol., Supp., Rev., and Addendum Numbers, if any.)
NUREG/CR-5948
LA-12459-MS

2. TITLE AND SUBTITLE
Hydrogen Mixing Studies (HMS):
Theory and Computational Model

3. DATE REPORT PUBLISHED
MONTH: Decemi ~ YEAR: 1992

4. FIN OR GRANT NUMBER
A7247

5. AUTHOR(S)
T. L. Wilson and J. R. Travis*

6. TYPE OF REPORT
Technical

7. PERIOD COVERED (Inclusive Dates)

8. PERFORMING ORGANIZATION — NAME AND ADDRESS (If NRC, provide Division, Office or Region, U.S. Nuclear Regulatory Commission, and mailing address; if contractor, provide name and mailing address.)

Los Alamos, National Laboratory
Los Alamos, New Mexico 87545

*Science Applications International Corporation
2109 Air Park Rd., SE
Albuquerque, NM 87106

9. SPONSORING ORGANIZATION — NAME AND ADDRESS (If NRC, type "Same as above"; if contractor, provide NRC Division, Office or Region, U.S. Nuclear Regulatory Commission, and mailing address.)

Division of Systems Research
Office of Nuclear Regulatory Research
U. S. Nuclear Regulatory Commission
Washington, DC 20555

10. SUPPLEMENTARY NOTES

11. ABSTRACT (200 words or less)

This report documents the governing physical equations and computational model of HMS (Hydrogen Mixing Studies), a finite-volume computer code for solving transient, three-dimensional, compressible, Navier-Stokes equations for multiple gas species. The code is designed to be a best-estimate tool for predicting the transport, mixing, and combustion of hydrogen and other gases in nuclear reactor containments and other facilities. An analysis with HMS will result in the pressure and temperature loadings on the walls and internal structures.

HMS can model geometrically complex containment systems with multiple compartments and internal structures. It can calculate gas behavior of low-speed buoyancy-driven flows, of diffusion-dominated flows, and during deflagrations. The code can model condensation in the bulk fluid regions; heat transfer to walls and internal structures by convection, radiation and condensation; chemical kinetics of combustion of hydrogen or hydrocarbons; and fluid turbulence. Heat conduction within walls and structures is one-dimensional.

In HMS, the computational domain is discretized by a mesh of parallelepiped cells in either Cartesian or cylindrical geometry, where primary hydrodynamic variables are cell-face-centered normal velocity and cell-centered density, internal energy, and pressure. A linearized Arbitrary-Lagrangian-Eulerian (ALE) method is used for approximating the solution to the mass, momentum, and energy conservation equations.

12. KEY WORDS/DESCRIPTORS (List words or phrases that will assist researchers in locating the report.)
Hydrogen, mixing, containment systems, computational modeling

13. AVAILABILITY STATEMENT
Unlimited

14. SECURITY CLASSIFICATION
(This Page)
Unclassified
(This Report)
Unclassified

15. NUMBER OF PAGES

16. PRICE

NRC FORM 335 (2-89)


Federal Recycling Program